CHAPTER 5

FABRICATION, COUPLING AND NONLINEAR OPTICS OF ULTRA-HIGH-Q MICRO-SPHERE AND CHIP-BASED TOROID MICROCAVITIES

Tobias J. Kippenberg, Sean M. Spillane, Deniz K. Armani, Bumki Min, Lan Yang and Kerry J. Vahala

Department of Applied Physics, California Institute of Technology
Pasadena, CA 91125

Surface-tension-induced micro-cavities (STIMs) possess ultra-high-Q values (typically greater than 100 million) within micron-scale dimensions. Their "whispering-gallery" type optical modes are confined by continuous total internal reflection at the dielectric cavity interface. Silica micro-spheres are a well-known example of STIMs, which possess record Q values in excess of 10^9. In this chapter we will discuss a novel type of ultra-high-Q (UHQ) microcavity fabricated on a microelectronic silicon chip, which allows a level of integration and control previously not available in the UHQ regime. The device merges concepts used in traditional surface-tension-induced microcavity fabrication with standard microfabrication techniques to combine UHQ with wafer-scale integration. We have studied the quality-factor (Q) and modal structure of these toroidally-shaped microcavities and have observed Q-factors exceeding 100 million, similar to values achieved in micro-spheres. Investigations of optical coupling to UHQ microcavities using tapered, optical fibers are also described and show that highly efficient coupling can be obtained, with efficiencies in excess of 99%. Ultra-high-Q combined with micron-scale modal volumes and the ability to efficiently transfer optical power both to and from the whispering gallery modes, leads to extremely high circulating intensities. These intensities can easily exceed the thresholds for all common nonlinear phenomena in silica. This has allowed us to observe a variety of nonlinear oscillations at threshold levels several orders lower than in any prior work and typically in the micro-Watt regime. In particular, stimulated and cascaded Raman scattering and parametric oscillation are studied both experimentally and theoretically. The ability to dope silica with rare earths to create on-chip silica micro-lasers in the important 1500 nm band is also investigated. Finally, we review the regime of strong modal coupling induced by backscatter effects within the resonator, and examine how backscattering modifies waveguide coupling properties including a change of the condition of "critical coupling".

1. Introduction

This Chapter reviews the fabrication, fiber-optic coupling and nonlinear optical properties of UHQ STIMs, including a recently-developed chip-based toroidal device. The pioneering work of Braginsky and Ilchenko[1] demonstrated the unique properties of silica micro-sphere-STIMs to confine light for extended periods of time. Silica micro-spheres exhibit record Q values due to both the low intrinsic material loss of silica in the visible and near infrared and the nanometer-scale surface smoothness of the resonator dielectric interface[2]. The highest Q to date observed in silica micro-spheres has been $9x10^9$ (and a cavity Finesse of $2.3x10^6$ at a wavelength of 850 nm) which is close to the fundamental material absorption limit at this wavelength[3]. These attributes have inspired numerous applications of micro-spheres in fundamental and applied areas. The long photon storage times are especially attractive for cavity QED experiments. The interested reader is referred to the chapter by S. Haroche and co-workers in the previous volume of this series (reference [4]) as well as to recent reviews [3, 5]. Furthermore silica micro-spheres can be used to create low-threshold lasers [6, 7] and nonlinear oscillators [8]. It is also important to note that more generally, liquid droplet STIM nonlinear oscillators were pioneered by R. Chang and co-workers [9-11] and A. Campillo and co-workers [12, 13] nearly two decades ago. More recently micro-spheres have also entered the field of biochemical sensing [14] as optical transducers with high sensitivity. Despite the advantageous properties of UHQ silica micro-spheres they do have several significant disadvantages. These include the fact that their physical characteristics are difficult to control during fabrication and that their mode spectrum, while well-studied[15], is highly complex and varies in a way that is strongly dependent upon subtle variations in the eccentricity of the sphere. Finally, and most significant, is that sphere fabrication lacks all of the desirable features of wafer-scale processing, now the standard method of fabrication employed for low and moderate Q microcavity applications. These advantages include precise lithographic control and reproducibility of dimension, as well as fabrication parallelism and the potential for integration with additional functionality such as electrical or micromechanical devices.

In short, wafer-processing techniques offer a far more powerful approach to fabricating micro-cavities. Photonic crystal defect cavities, micro-post structures,

and ring geometry whispering gallery devices at moderate Q levels are now fabricated routinely using wafer-scale technology as described in the companion chapters by Little, Scherer, Steier and Yamamoto in this book. Reported Q-factor results have ranged from 13,000[16] in InGaAs microdisks, to 130,000 in polymer rings[17], to a record value of 3 million in a silica microdisk reported by our group and described in this chapter. However, these Q-factors are several orders of magnitude lower than those found in surface-tension-induced micro-cavities, since the nanometer-scale surface finish required for ultra-high-Q has not been attainable using wafer-scale processing.

Despite tremendous progress in the the UHQ regime application space (Q typically greater than 100 million – see [2, 5]),   wafer-based UHQ devices have remained elusive. In this chapter, we also present and explore the properties of a chip-based (planar) STIM devices in the form of a micro-toroid which combine for the first time the advantages of wafer-scale processing and ultra-high-Q [18]. These cavities are made by combining conventional micro-fabrication techniques with a laser-assisted reflow process to achieve the atomic-scale surface finish characteristic of STIMs. We have observed Quality factors of up to 500 million in these structures, similar to values reported and measured for silica micro-spheres. The mode structure of these micro-cavities exhibits a strongly-reduced mode density compared to a micro-sphere of the same size. A further unique property of micro-toroids is the ability to reduce their optical mode volume significantly below those of micro-spheres of comparable diameter. This property is particularly important for nonlinear optical and cavity QED experiments.

In another focus of this chapter, we also review the coupling and transfer of optical power to both micro-spheres and micro-toroids on-a-chip using tapered optical fibers[19, 20]. Using tapers we have demonstrated the efficient excitation of whispering-gallery-modes and observed the condition of "critical coupling" [19]. We also show that in the regime of ultra-high-Q the coupling properties are altered due to back-scatter-induced modal coupling of the whispering-gallery-modes[21]. The "ideality" of the taper-resonator junction is also studied and characterized using a new method [22]. The junction is shown to exhibit an extraordinarily high ideality in terms of linking a target resonator mode with the fundamental taper mode. This property has potential importance in quantum optical studies where low-loss optical fiber is proposed for transport of non-classical states and correlations of light[23].

The efficient transfer of optical power and accurate control of coupling strength using the tapered fiber method when combined with the ultra-high-Q and microscale nature of the whispering gallery modes enables the resonant buildup of very high circulating intensities leading to a variety of nonlinear

optical processes.The regime of very-high circulating intensities – both in silica microspheres and in micro-toroids - where the nonlinear interaction of light and matter becomes prominent is reviewed in section 5. In studying these processes, the fiber taper serves to both couple pump power as well as to extract newly generated waves thereby allowing precise study of nonlinear optical effects. For appropriate coupling and Q conditions nonlinear oscillation at microwatt-level fiber-coupled power levels is observed [8, 24]. Near theoretical efficiencies are possible due to the high-ideality of the taper-resonator junction. As such these systems offer both a well-controlled laboratory in which to study nonlinear phenomena, and also a potentially practical on-chip nonlinear optical source. One such nonlinear effect is stimulated Raman scattering, wherein the light field interacts with the material by way of a vibrational state (an optical phonon) [25]. We have observed this effect and created fiber-coupled Raman micro-cavity lasers using both a micro-sphere[8] and a micro-toroid on-a-chip. In addition to stimulated nonlinearities (i.e. Raman) we have also observed a second class of nonlinear interactions (parametric interactions). Whereas stimulated processes such as Raman are intrinsically phase matched, parametric oscillation requires stringent phase matching conditions causing the stimulated Raman nonlinearity to dominate micro-cavity nonlinear optics. However, we show that by controlling micro-toroid cavity geometry a transition from stimulated Raman to parametric oscillation can be achieved, allowing for the first time the observation of the Kerr-induced parametric oscillation in a micro-cavity.

In section 6, we review the application of both spheres and micro-toroids as lasers employing rare-earth doped silica. For the same reasons described above in conjunction with nonlinear oscillators, these devices are important because of their high-differential efficiency and low threshold operation. As was also true for the toroid-based nonlinear oscillators, rare-earth doped toroids have the significant advantage of being chip-based devices that are directly coupled to optical fiber. The processing developed to create these lasers uses a novel sol-gel based approach in which erbium is coated upon the device and subsequently selectively densified at the toroid periphery. The process, itself, thereby allows a precise application of the erbium dopant where it is required.

Finally, we will conclude the chapter with an outlook section.

2 Ultra-high-Q micro-cavity fabrication and background

2.1. Micro-spheres

The optical modes of spherical cavities have been intensively studied, starting with Mie [ref]. Here we provide only a brief review of some of the basic properties of the micro-sphere mode structure. The interested reader is referred to detailed reviews such as found in ref [15, 26] The mode structure of micro-sphere resonators is well-known and follows from solving the spherical wave equation. Owing to spherical symmetry (and in analogy with the solutions of a hydrogen atom), modes are characterized by angular (ℓ), azimuthal (m), radial (n) and polarization (p) indices. Perfect spherical symmetry guarantees degeneracy with respect to the index m, however, in practice this $2\ell+1$ degeneracy is never achieved due to eccentricity-induced splitting. The resulting "spherical" mode spectrum is therefore highly complex and strongly dependent upon fabrication-induced eccentricity. Whispering gallery modes, like their acoustical analogues [27], are a class of modes that execute "orbits" near the surface of the sphere. Their near surface trajectories make their Q strongly dependent upon interfacial blemishes and surface roughness, however, their radiation leakage or tunneling is the lowest of all modes within the sphere and hence, in cases where the surface is exceptionally smooth, these modes also exhibit the highest quality factors. Indeed, radiation tunneling is a negligible component of loss in STIM silica spheres for sphere diameters in excess of 20-30 μm. So-called "fundamental" whispering gallery modes are ring shaped orbits and correspond to the spherical harmonic solutions ℓ=m. For the case of the fundamental radial index they exhibit the smallest modal volume and as such are interesting in studies of cavity QED and nonlinear optics. Figure 1 shows green luminescence from a fundamental whispering gallery mode in a micro-sphere.
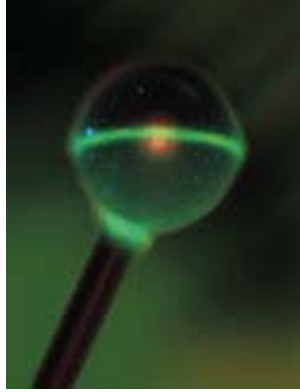
Fig. 1. Main graph: Optical micrograph of an Erbium-doped, micro-sphere resonator that is approximately 70 μm in diameter. The green luminescence originates from Erbium up-conversion and indicates that the modal distribution of the light is in the fundamental whispering gallery sphere mode. Visible in the bottom of the picture is the fiber stem, which is used to position the micro-sphere. Micrograph courtesy of M. Cai.

The ultimate obtainable Q-factor for a micro-spherical cavity has been intensively studied by several groups, with the highest reported Q to date of 9×10^9 at a wavelength of 850 nm. This value is close to the theoretical absorption limit of silica at this wavelength, however, for slightly longer wavelengths in the telecom band around 1550 nm, the theoretical limit imposed by material loss is around 100 billion.

The micro-spheres described in this chapter were fabricated by heating the tip of a tapered telecommunication fiber using a 10 Watt CO_2 laser. Silica is highly absorptive at 10.6 μm and can be readily melted by this method. The surface tension of the molten tapered glass tip causes the end to form a near-spherical shape, with residual eccentricities of typically a few percent. The un-melted portion of the optical fiber taper serves as a stem allowing convenient positioning with respect to the fiber-taper coupler as explained in later sections.

2.2 Fabrication of ultra-high-Q micro-toroids on-a-Chip.

Microtoroids are silica resonators on a silicon chip and their fabrication is described in this section. As noted in the introduction, micro-toroids enable access to the desirable ultra-high-Q performance of micro-spheres but in a design that is wafer based and that takes advantage of process control and parallelism not available with micro-spheres. The planar nature of these structures also restricts azimuthal degrees of freedom, rendering their mode spectrum far

simpler than that of a sphere. Fabrication of micro-toroid cavities on a chip proceeds as described in reference [18] in three basic steps: creation of a silica disk by a combination of lithography and pattern transfer, isolation of the disk periphery by selective undercut of the substrate, and finally, selective reflow of the disk material using a CO_2 laser to create the microtoroid. The process steps are illustrated in Figure 2.
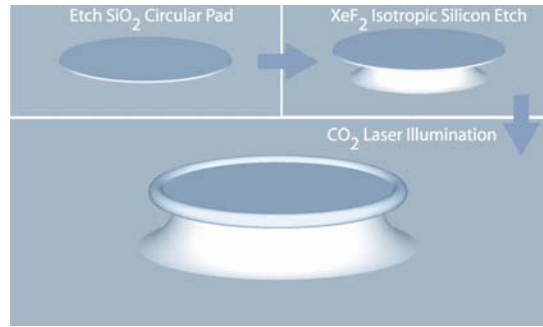

Fig. 2. Illustration of the process sequence used to fabricate silica toroidal micro-cavities on-a-chip. First, silica disks are created by lithography and etching, second, the silica disks are undercut using an isotropic silicon etch, and third, the silica disks are surface-normal-irradiated using a CO_2 laser which causes the disk to melt and collapse into a toroid-shaped form.

Further details of the fabrication process are as follows. First, photolithography using standard photo-resist is performed on a silicon wafer containing a thermally-oxidized surface layer to create circular photo-resist pads. The diameter of the photo-resist pads is chosen so as to be larger than the desired diameter of the toroid, since silica is consumed in the reflow process. After hard bake of the photoresist pads, circular disks are etched into the silica using buffered hydrofluoric acid. As the optical modes of the disk structure reside at the perimeter of the disk, the silica disks must be isolated from the high-index silicon to prevent leakage of optical energy into the substrate. This is achieved in the second step by using the silica disks as a etch mask for a silicon etch. An isotropic, selective, silicon etch employing XeF_2 gas at 3 Torr is used for this purpose. This process selectively removes the silicon, leaving circular silica disks on nearly-circular silicon support pillars. Figure 3 is a scanning electron micrograph of the resulting structure. The inset of figure 3 is an optical micrograph of the structure and also shows a fiber taper coupled to the resonator. The above process flow leaves lithographic blemishes at the all-important cavity-mode boundary, in many cases visible with an optical microscope.
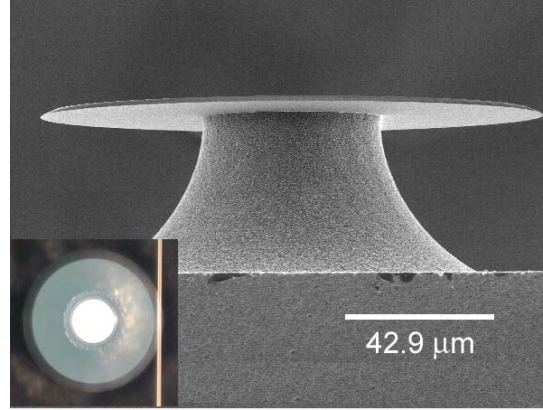
Fig. 3. Scanning electron micrograph of a silica micro-disk structure on a silicon wafer. The inset is a top-view optical micrograph of the structure coupled to a tapered fiber from the side.

The disks fabricated in this way exhibit whispering-gallery-type modes located near the disk periphery. Under optimal processing conditions we have measured Q-factors up to 3×10^6 in these structures[28], believed to be limited by lithography and etching. Therefore, to obtain UHQ performance further sample processing is necessary to obtain the nanometer-r.m.s (root mean square) surface roughness typical of STIMs[2].
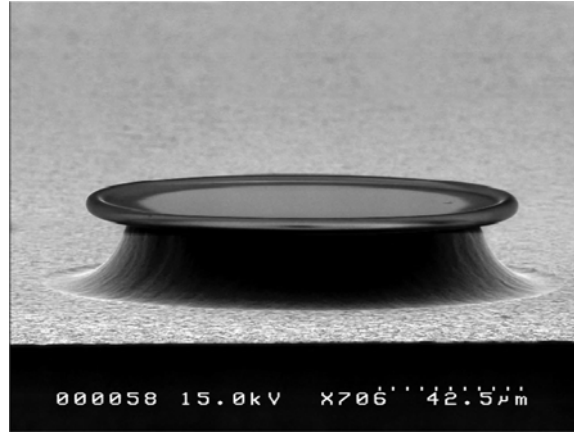

Fig. 4. Scanning electron microscope image of a 90-μm-diameter silica micro-toroid on a silicon chip. The initial silica disk ("perform") diameter was 160-μm and 2-μm thick, with the reduction in diameter due to formation of the toroid perimeter.

In order to achieve an exceptional surface finish a processing step is introduced that reflows the undercut silica disks without affecting the underlying silicon support pillar. This is accomplished by surface-normal irradiation of the disk ("preform") with a CO_2 laser (10.6-μm wavelength), similar to techniques once proposed for integrated-circuit planarization[29]. The laser beam intensity follows a Gaussian profile centered on the disk with a width exceeding that of the silica preform. Irradiation of the disk with laser intensities typically less than 100 Mega-Watts/cm^2 leads to melting and collapse of the silica at the disk periphery and not over the silicon post. The reason for this effect is that silicon has a far weaker absorption constant than for silica at 10.6 μm and additionally is 100-times more thermally conductive than silica. This leads to the silicon pillar staying significantly cooler (and physically unaffected) throughout the reflow process, allowing it to serve as a heat sink for optical power absorbed in the silica disk. An additional factor in the reflow process is the strong temperature dependence of the silica absorption [30], which increases substantially with temperature so that melting occurs abruptly with increasing laser fluence through a thermal runaway process.

Several methods have been investigated to control the final toroid shape and size in the reflow process. A first method uses continuous laser irradiation. In this case, the disk collapses and toroid formation is self-quenched by a combination of thermal conduction through the silicon pillar and the reduced cross section for absorption of CO_2 radiation. In this continuous-illumination formation process, the final toroid thickness (minor diameter) is determined by the preform diameter, pillar diameter and oxide thickness. Alternatively, in a second method, the reflow process can be interrupted prior to the self-quenching point by pulsed laser irradiation, which produces a toroid with a final diameter in between the disk and silicon pillar diameter. The structure in figure 4 has been created using this method. The silica disk used in this case had a 2 μm thickness and an initial diameter of 160 μm. During irradiation the diameter of the disk was reduced to 120 μm and the consumed silica formed a 7-μm-diameter toroid-shaped perimeter. We also note that due to the long absorption length in silica at room temperature for CO_2 laser radiation (approx 35 μm [30]), the required laser intensity to initiate disk collapse is increased significantly when using thinner oxides. Because it might not always be desirable to control the final toroid diameter by allowing complete collapse (i.e., 1st method) or through interruption of collapse, an alternative method of control was investigated as described below.

2.3 Toroid dimensional control by preform design

Increased lithographic control over the toroid geometry can be achieved by suitable design of the silica disk preform. Due to the thermal runaway effect, the thickness of the preform is an important parameter determining the required flux of CO_2 laser illumination to initiate silica reflow and toroid formation. As noted above, for thin oxide layers the required flux is strongly increased, and thus by using a variable preform thickness profile, the temperature distribution of the silica in the laser illumination process can be controlled. For example, an annular preform (i.e., thicker at the perimeter) will be preferentially heated at the perimeter, where the oxide thickness is large. We have found that not only does this mean that the melt initiates in the annulus, but significantly it is prevented from proceeding into thinner interior. The left panel of figure 5 is an optical micrograph of an annular preform, featuring a thick rim at the perimeter (2 μm), and a thinner, interior disk (1 μm). In order to fabricate this structure two consecutive lithographic steps and buffered HF oxide etching were performed. The right panel in figure 5 shows the structure after pulsed laser illumination. The outer annulus region preferentially melts and surface tension causes it to form a toroid. The process is observed to self-quench when the inner toroid diameter reaches the inner annulus diameter, and, significantly, prior to reaching the silicon pillar, The advantage of this fabrication technique is that the amount of material used to form the toroid as well as the inner diameter of the toroid micro-cavity can be accurately controlled by lithography. In addition, the supporting disk structure can be made very thin, which thereby increases the optical confinement of the modes within the toroidal periphery.
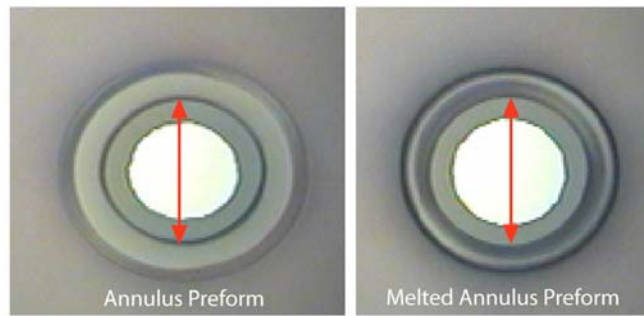

Fig. 5. An annular preform can be used to control the dimensions of the toroid. The left panel shows an annular preform prior to melting and the right panel shows the preform after irradiation. The CO_2 laser radiation selectively melts the thicker annulus perimeter, leaving the thinner interior disk unaffected.

3.   Coupling to ultra-high-Q micro-cavities using tapered optical fibers

Efficient coupling of UHQ whispering-gallery modes is a prerequisite for studying both micro-sphere and micro-toroid cavities and is important in studies that either require low loss or efficient power transfer into and out of a cavity mode. To couple light into micro-spheres several techniques have been used, ranging from free-space illumination to evanescent coupling techniques. Since the fundamental whispering-gallery modes are confined near the surface of the micro-sphere, evanescent coupling techniques can provide a powerful means of control of the coupling properties. A common technique used to excite micro-sphere resonances is prism coupling, where the evanescent field of a laser beam, which undergoes total internal reflection in a prism, is brought into overlap with the whispering-gallery mode[26, 31, 32]. We describe here an alternate method that enables high efficiency coupling directly from optical fiber[19]. Additional details on this method which relies upon the formation of a narrow tapered segment within the optical fiber is provided in refs [19, 20, 26]

Tapered optical fibers allow both efficient excitation and extraction of optical power from the same fiber, while maintaining fiber-optic compatibility. Using tapered optical fibers we have achieved very efficient excitation of whispering gallery modes and observed the condition of 'critical coupling'. Of even greater significance is that the fiber taper junction is highly "ideal" meaning that it's behavior closely approximates a perfect two-mode coupler[22]. Indeed, it is not an exaggeration to say that the ideality and insertion loss of taper junctions vastly exceed what is considered typical for optical coupling to micro-resonators. As such they are potentially important junctions in systems requiring ultra-low loss coupling to optical fiber, such as in quantum optics and quantum information studies [23, 33-38]. They are also inherently fiber compatible, giving them great utility in the laboratory for test and measurement. They are also useful when studying active and nonlinear micro-resonators, since the newly generated waves can be extracted through the same fiber that provides the pump excitation. This will be discussed further in section 5.
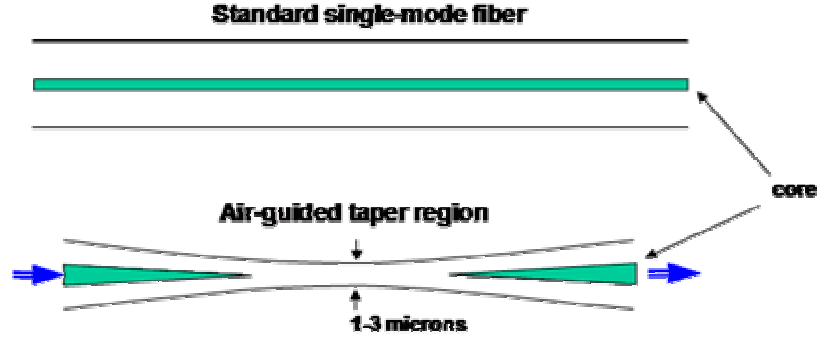
Fig 6. Schematic showing a standard telecommunication fiber and a tapered optical fiber.

Tapered optical fibers are made by heating a single-mode fiber (typically SMF-28) with a torch and slowly pulling the fiber apart until a waist region only a few microns in diameter is created. By maintaining an adiabatic taper profile [20, 39] an initially-launched fundamental, fiber mode is converted to an air-guided, fundamental, taper mode and vice versa upon propagating through the tapered region. In principle, the loss arising from higher-order mode coupling or radiation leakage can be made arbitrarily small. Tapers used in our work typically have losses of a few tenths of a dB. We have analyzed the taper waist diameter in a scanning-electron-microscope and measured taper sizes of less than 1 μm, while maintaining loss levels of less than 0.1 dB.

We have studied taper excitation of micro-sphere WGMs in the optical telecommunication range. To excite the fundamental whispering gallery mode of the micro-sphere, the taper is brought close to an equator of the sphere, where the fundamental modes are confined. Coupling into the micro-sphere requires that three conditions are satisfied. First, the evanescent field of the fiber taper and the micro-sphere mode exhibit spatial overlap, second, the frequency of the excitation wave must be resonant with a target WGM of the sphere, and finally the propagation constants of the taper and whispering-gallery mode need to be matched to some extent (i.e., phase matched). As will be described below, the last requirement can be relaxed in cases where the taper is highly single mode and where the resonator is UHQ. The overall coupling strength depends on the overlap of the taper with the sphere mode (which varies typically exponentially with the air gap between the resonator and the taper) as well as on phase-matching. Energy transfer is most efficient when the propagation constants of the fundamental taper mode and the micro-cavity WGM are equal. Phase-matching is accomplished in practice by matching the taper propagation constant to the WGM's propagation constant through change of the taper waist diameter. In

experiments, the coupling is also controlled by varying the gap distance using a three-axis piezoelectric stage (step resolution of 20-nm) to accurately position of the taper with respect to the micro-cavity. We found it helpful in our experiments to keep the taper under slight tension to minimize the influence of vibrations. We also discovered the particular suitability of this method to couple micro-toroids on-a-chip. Since the toroidally-shaped perimeter of these cavities lies typically only a few tens of microns above the surface of the planar substrate, coupling using tapered fibers is ideally suited to this geometry, whereas bulk couplers such as prisms present additional alignment difficulties. The other advantages of fiber-taper coupling will be explained in more detail in the following sections where tapered fibers are used to excite micro-toroid whispering gallery modes and to study nonlinear optical effects in these structures. Figure 7 shows a micro-sphere and micro-toroid side-coupled to a tapered fiber.
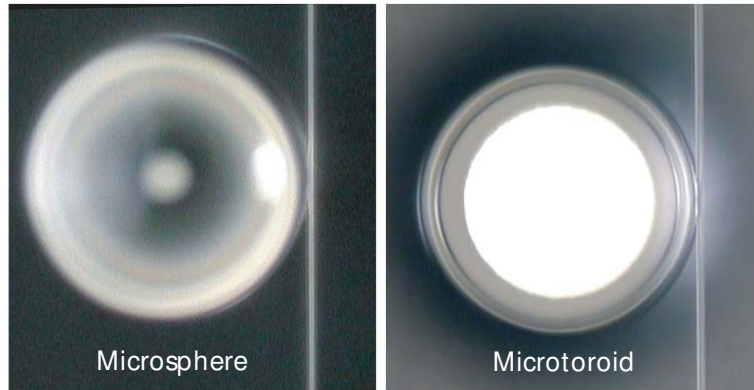

Fig. 7. An optical micrograph showing a tapered fiber that is side-coupled to a micro-toroid on-a-chip (right) and a microsphere (left). The micro-toroid has a diameter of approximately 90 μm and has a supporting silicon pillar (appearing white in the image). The microsphere in the image has diameter of ca. 80 μm.

As discussed above, a tapered fiber converts the fundamental fiber mode into an air-guided taper mode. The taper section near the micro-cavity junction can locally be described as a silica rod with guiding determined by the index of refraction of the original fiber cladding and the external environment (typically air; index of refraction near unity). For the taper diameters used in this work to couple to WGM's (1.5-3 μm), a simple calculation shows that the local waveguide is multimode. Even though the adiabatic taper guarantees launch of

the fundamental taper mode from the input side to the micro-resonator, the presence of multiple output waveguide (and radiation) modes means that, in general, a resonator mode can couple to all of the supported local radiation/waveguide modes of the taper. Any power which couples into modes other than the fundamental taper mode will be lost upon transition of the waveguide back to single-mode fiber. Nonetheless, we are able to show that with proper choice of taper diameter, this parasitic, non-intended coupling can be reduced to a negligible level, rendering the taper junction highly efficient for coupling both to and from the resonant mode[22].

To substantiate this claim, we have developed a technique to measure parasitic junction coupling losses, defined as any loss that occurs by way of unintended coupling. The junction performance is quantified in terms of the degree to which the fiber-taper/resonator junction behaves as a true single-mode/single-mode coupler, expressed as the *ideality* of the junction.

The coupling between a multimode waveguide and a resonator (illustrated in fig. 8) can be modeled using a simple approach valid for weak coupling and small internal resonator loss. Under these conditions, the contributions of waveguide-induced cavity loss and intrinsic cavity loss are separable[40]. These conditions are met for the experimental configurations presented in this chapter. Under these assumptions, the internal cavity field ("a") is determined by accounting for all sources of cavity loss and excitation, and can be described by:

$$\frac{da}{dt} = i\Delta\omega a - \frac{1}{2}\left(\frac{1}{\tau_0} + \frac{1}{\tau_{rad}^e} + \sum_{i=0}\frac{1}{\tau_i^e}\right)a + i\sqrt{\frac{1}{\tau_0^e}}s$$

(1)

Here τ_0 is the intrinsic resonator photon lifetime, τ_{rad}^e is the lifetime for coupling/scattering to radiation modes, and τ_i^e denotes the coupling lifetime for coupling to each supported waveguide mode (τ_0^e represents the fundamental waveguide mode which is always present). The last term gives the excitation of the cavity due to only the fundamental waveguide mode with amplitude denoted by s under adiabatic tapering conditions. The transmission past the resonator consists of an interference of the transmitted optical field (i.e., that component that did not couple to the resonator) plus the field coupled out of the resonator into the fundamental taper mode (as power in all other modes is lost in the adiabatic transition), and is given by:
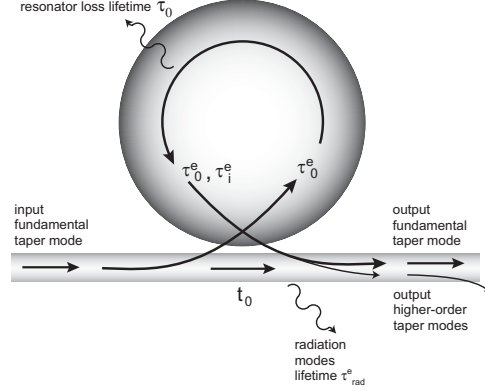
Fig. 8. Illustration showing the various, coupling mechanisms within a waveguide-resonator system. The input field (single-mode due to adiabatic launch conditions) excites the resonator with a coupling lifetime τ^e_0 and transmitted amplitude t_0. The resonator mode couples into radiation modes with lifetime τ^e_{rad}, and all supported waveguide modes with lifetime τ^e_i. The intrinsic resonator lifetime is given by τ_0.

$$T = \left| t_0 + i\frac{a}{s}\sqrt{\frac{1}{\tau^e_0}} \right|^2 \tag{2}$$

In steady state, the waveguide transmission on resonance can be expressed in the form

$$T = \left(\frac{1-K}{1+K}\right)^2 ;\ K \equiv \frac{\left(\dfrac{1}{\tau_0} + \dfrac{1}{\tau^e_{rad}} + \sum_{i \neq 0}\dfrac{1}{\tau^e_i}\right)^{-1}}{\tau^e_0} \equiv \frac{\tau'_0}{\tau^e_0} \tag{3}$$

where K denotes a dimensionless coupling parameter. Briefly, K=1 is denoted as critical coupling, K>1 as over-coupled and K<1 as under-coupled[40]. The transmission expression is identical to that expected for a perfect single-mode to single-mode coupler, provided that the resonator intrinsic loss lifetime is taken as the "effective" (primed) lifetime defined above in the last equality. This interpretation is intuitive as any power not coupled into the fundamental mode of the output waveguide can be considered a resonator-specific loss when looking at the system as a whole. Thus the effective intrinsic lifetime has a contribution due to the actual resonator intrinsic lifetime (independent of coupling) as well as a lifetime associated with various components of parasitic coupling. These contributions can be separated by decomposing K as follows:

$$K^{-1} = K_I^{-1} + K_P^{-1} \qquad (4)$$

where:

$$K_P \equiv \frac{\left(\dfrac{1}{\tau_{rad}^e} + \displaystyle\sum_{i \neq 0} \dfrac{1}{\tau_i^e}\right)^{-1}}{\tau_0^e} \text{ and } K_I \equiv \frac{\tau_0}{\tau_0^e}$$

and where K_I and K_P are defined as the intrinsic and parasitic coupling parameters, respectively. To describe the degree to which the coupling junction behaves as a single-mode coupler, we define the junction ideality[22], where ideality is the ratio of power coupled into the desired fundamental waveguide mode to optical power coupled into all junction-related modes (both parasitic and fundamental mode) and is given by,

$$I \equiv \frac{1}{1 + K_P^{-1}} \qquad (5)$$

The ideality ranges from zero (no coupling at all into the desired mode) to unity (perfect single-mode coupler). Measuring the ideality of a waveguide-resonator system, thus requires one to accurately determine the parasitic coupling K_P. While, in principle, K_P can be determined from the transmission expression, coupled with knowledge of the intrinsic and coupling lifetimes, a more sensitive technique to measure K_P is to note that parasitic coupling will in general vary as the taper-resonator gap is varied. This variation will produce an observable deviation in the coupling parameter K from the ideal case that can be used to infer K_P. To see that this is true, consider the dependence of coupling strength K on gap. By inverting equation 3 we obtain,

$$\left(\frac{1 \pm \sqrt{T}}{1 \mp \sqrt{T}}\right) = K = \frac{\left(\dfrac{1}{\tau_0} + \dfrac{1}{\tau_1^e e^{\alpha_1 x}}\right)^{-1}}{\tau_0^e e^{\alpha_0 x}} \qquad (6)$$

where the upper signs are taken for transmission values in the over-coupled regime, and the lower signs in the under-coupled regime. The second equality follows from equation 4 and by noting that the coupling lifetimes associated with coupling to the various taper modes will vary exponentially with resonator-waveguide separation (τ-bar represents the lifetime at resonator/waveguide contact and α represents the rate of increase of lifetime with separation). In addition, it has been assumed in this equality that the parasitic coupling parameter is dominated by coupling to a single higher-order waveguide mode.

This assumption is valid for the range of taper sizes typically investigated in this chapter. As demonstrated below, by plotting K on a logarithmic scale versus the gap distance, K_I and K_P can often be identified. This is possible because the spatial decay rate of the higher-order fundamental mode is distinct from that of the fundamental, causing K_P to be a line with a slope less than that of K_I. If the degree of parasitic coupling is comparable to or greater than the intrinsic resonator loss over the range of gaps measured, then the roll-off of K has asymptotes determining K_I and K_P. If, however, parasitic coupling is less than intrinsic loss, the parasitic coupling is not observable and only a lower bound on K_P (and thus ideality) can be established.

We have experimentally investigated the ideality of a fiber-taper/silica microsphere system using the above approach for WGM resonances around 1550 nm. The transmission data are obtained by normalizing the on-resonance power transmission with the power transmitted through the taper alone (i.e. in the absence of a resonator). The ideality in this measurement was determined for several taper diameters. Figure 9 shows the resultant coupling parameters K plotted vs. taper-sphere gap for local taper diameters of 1.2 μm, 1.35 μm, and 1.65 μm (measured by an scanning electron microscope).
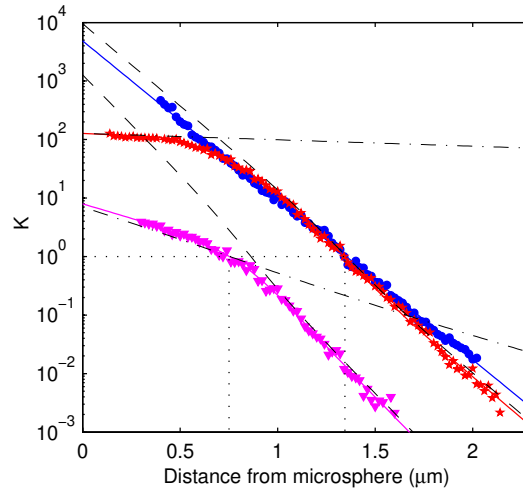

Fig. 9. Coupling parameter K vs. taper-sphere gap for taper diameters of 1.2 μm (circles), 1.35 μm (stars), and 1.65 μm (triangles). The lower ideality as taper size increases is manifested as an increased roll-off of the data as gap distance is reduced. The dashed and dash-dotted lines represent the intrinsic coupling parameter K_I and the parasitic coupling parameter K_P, respectively. The dotted lines mark the critical point for each data set.

The data clearly show that taper diameter strongly influences the coupling parameter versus gap dependence. As taper diameter increases, the increased influence of higher-order mode coupling (a result of the decreased phase-mismatch between the fundamental taper mode and the next higher-order mode) leads to a strong roll-off of K with decreasing gap from the expected linear relation representing perfect ideality. A fit using equation 6 shows excellent agreement, confirming that the dominant contribution to non-ideality in this measurement is from coupling to a single higher-order taper mode. Using the fit, both K_P and K_I can be extracted (dash-dotted and dotted lines in figure 9, respectively), which allows determination of the junction ideality versus gap distance. The 1.65 μm taper data yield a value for ideality ranging from 88% at taper-sphere contact to 13% at a gap distance of 1.5 μm. The next smaller taper size has an improved ideality value ranging from 99% at contact to 98% at the 1.5 μm gap. For the smallest taper size measured, the behavior appears completely ideal. As it is not possible to infer a dependence of K_P on taper-sphere gap, due to the finite loss of the resonator, only a lower bound on ideality at contact can be established for this case by using the value of K at taper-sphere contact. In this case we obtain a lower bound of ideality of 99.98%.

One consequence of reduced ideality is a shift of the critical coupling point due to the increased parasitic loss. This can be seen in figure 9 (all data sets taken using the same resonator and hence resonator intrinsic loss is unchanged from set-to-set). For perfect ideality, the critical point should occur at the gap distance where $K_I = 1$ [40]. Inspection of the data for the largest taper size reveals that reduced ideality results in a shift of the critical point towards smaller gap distances. The critical point is essentially unaffected for the two smaller taper diameters, as a result of the large ideality values at critical coupling. Considering the large taper data once more, the critical point is shifted by 100 nm with respect to its position in the ideal case. An implication of this shift is that a non-ideal coupler can lead to an under-estimation of the intrinsic cavity Q factor when using the measured Q at critical coupling to infer the actual intrinsic resonator Q (as is commonly done either by line-width measurements or cavity ring-down). The data also demonstrate that the ideality of the junction actually decreases as the taper-sphere gap is increased. This, at-first-sight counter-intuitive fact, is the result of the slower evanescent decay of higher-order taper modes. This also implies, that if high ideality is to be achieved in the under-coupled or critically coupled condition, high ideality at contact is a prerequisite.

We have also investigated the absolute ideality attainable in this system by attempting to maximize the value of K through strongly overcoupling to an ultra-high-Q microsphere as shown in Figure 10.
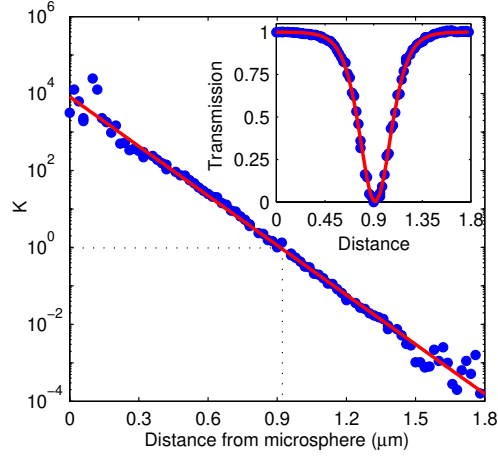
Fig. 10. Coupling parameter K vs. taper-sphere separation for a 65-µm-diameter micro-sphere showing highly ideal behavior. A fit assuming an ideal coupler (solid line) gives a lower bound on ideality of 99.99% in contact. The inset shows the original transmission data, with over-coupled transmission exceeding 99.95%.

Numerical calculations based on a modified coupled-mode theory verify that the observed slope of K is consistent with the expected ideal behavior. Using the approach described above, an extrapolated ideality value in contact exceeding 99.99% is obtained. Using a more conservative estimate based upon the actual measured data points in the vicinity of contact still results in a lower-bound value greater than 99.97%. This data includes all forms of taper insertion loss (e.g., even that associated with radiation mode scattering from juxtaposition of the taper and sphere). Thus this value provides an absolute determination of a physically realizable value. The original transmission data (inset) show that nearly complete over-coupling is obtained, with over-coupled transmission values exceeding 99.95%. The fact that fiber tapers can provide exceedingly low coupling loss to UHQ resonators allows great flexibility to study processes in micro-cavities where loss is highly undesirable. This includes applications in cavity QED [37] and quantum optics, and the study of active and nonlinear cavities as described below. Equally important is that this coupling is to optical fiber, the optical transport medium of choice. This last point cannot be over-emphasized as it enables experimental work to leverage the enormous investment in technology resulting from fiber communications.

3.1.   *Modal coupling in whispering-gallery-mode micro-cavities*

Whispering-gallery-type modes possess a natural 2-fold degeneracy due to the two possible directions of propagation (clockwise and counterclockwise). Haroche *et al.*[41] have observed breaking of this degeneracy in the regime of ultra-high-Q [41]   when the counter-propagating cavity modes are coupled through various mechanisms including Rayleigh scattering or scattering from surface defects at the dielectric boundary of the cavity [42]. When the mode scattering rate from such mechanisms exceeds the photon decay rates, caused either by intrinsic cavity loss or by waveguide coupling, one expects to enter a regime of "strong modal coupling" where lifting of the degeneracy (splitting of the resonant frequency into a doublet) can be observed. Curiously, many of the same mechanisms that are responsible for the intrinsic cavity loss will also tend to couple the counter-propagating modes. Hence, this mode-coupling is an effect that is a nearly inevitable consequence of entering the UHQ regime. Mode-coupling was theoretically investigated by Gorodetsky and it was predicted that in the so-called strong modal-coupling regime micro-resonators can act as narrow-band reflectors[32]. In this section we describe experimental observations of mode splitting and in particular the regime of strong modal coupling. We also show that in the regime of strong modal coupling a shift in the critical coupling point occurs. Understanding this shift is important in measurements of Q factor that occur in the presence of backscatter. Indeed, we provide an expression that enables the proper renormalization of Q in such circumstances. Furthermore, the waveguide-resonator coupling condition of maximum power transfer no longer coincides with the critical coupling point.

The equations of motion for counter-propagating (CCW and CW) modes that are coupled to one another as well as to a waveguide mode can be described by the couple-mode equations similar to those presented in reference [32]:

$$\frac{d\mathrm{a}_{cw}}{d\mathrm{t}} = \mathrm{i} \cdot \Delta\omega \cdot \mathrm{a}_{cw} - \frac{1}{2\tau}\mathrm{a}_{cw} + \frac{\mathrm{i}}{2\gamma} \cdot \mathrm{a}_{ccw} + \kappa \cdot \mathrm{s}$$

$$\frac{d\mathrm{a}_{ccw}}{d\mathrm{t}} = \mathrm{i} \cdot \Delta\omega \cdot \mathrm{a}_{ccw} - \frac{1}{2\tau}\mathrm{a}_{ccw} + \frac{\mathrm{i}}{2\gamma} \cdot \mathrm{a}_{cw}$$

(7)

Here "a" is the amplitude of the CCW and CW modes of the resonator and s denotes the input wave, which is selected to excite the CW mode. The excitation frequency is detuned by $\Delta\omega$ with respect to the resonance frequency ω_0 of the initially degenerate modes. τ is the total lifetime (i.e., that which accounts for

both intrinsic cavity loss as well as coupling loss to the waveguide) of photons in the resonator and is related to the quality factor by $Q = \omega \cdot \tau$. The coefficient κ denotes the amplitude coupling of the input wave to the CW mode of the resonator. The relation $\kappa = \sqrt{\tau_{ex}^{-1}}$ associates the coupling coefficient with a corresponding lifetime, such that $1/\tau = 1/\tau_{ex} + 1/\tau_0$[43]. The mutual coupling of the CCW and CW mode is described by a (scattering) rate $1/\gamma$. The degenerate WGMs couple to the waveguide in opposite directions and give rise to reflected (r) and transmitted (t) signals.

$$t = s - \kappa \cdot a_{CW}, r = \kappa \cdot a_{CCW}$$

(8)

The scattering to all modes other than the originally degenerate pair of modes is included in the overall cavity loss, as given by the intrinsic lifetime τ_0. In the presence of modal coupling, the new cavity eigenmodes are symmetric and anti-symmetric superpositions of the original CW and CCW modes centered around new eigenfrequencies $\omega_0 \pm 1/\gamma$ (having a linewidth of $1/\tau$ as illustrated in figure 11). For strong modal coupling the two new eigenmodes correspond to standing waves, similar to those in a Fabry-Perot resonator. To enable a more precise definition of strong intermode coupling, we introduce below the normalized intermode coupling parameter Γ [21] and the normalized coupling coefficient K (which is identical to the K_I parameter introduced in the previous section).

$$\textit{Modal coupling parameter: } \Gamma \equiv \left(\frac{\tau_0}{\gamma} \right),$$

(9)

$$\text{Normalized coupling parameter: } K \equiv \left(\frac{\tau_0}{\tau_{EX}} \right)$$

(10)

These normalized coupling coefficients describe the rate of modal coupling and waveguide-coupling with respect to the intrinsic cavity loss rate. The regime of strong modal coupling is characterized by $\Gamma \gg 1$ while, as noted earlier, the normalized coupling coefficient K describes the waveguide coupling regimes with K>1 over-coupled, K<1 under-coupled, and K=1 critically coupled[43].

We have observed the splitting of degenerate WGMs into doublets in both micro-sphere and micro-toroid resonators, and have investigated the modified coupling properties using the fiber-taper coupling technique. As noted earlier, doublets are prominent in UHQ micro-cavities since only minute amounts of scattering either from bulk Rayleigh or from surface imperfections are sufficient to cause easily observable mode coupling[42]. In experiments the taper contributes a negligible amount to the overall scattering (slight increase in mode

splitting of less than 5% while scanning the taper from under-coupled to over-coupled), confirming that scattering centers either intrinsic to the resonator or at the resonator surface dominate. The inset to figure 11 is a photomicrograph of a micro-sphere (diameter ca. 70 μm) coupled to a tapered fiber. The coupling strength τ_{ex}^{-1} is adjusted by varying the taper-resonator gap distance in steps as small as 20 nm. A 1.55 µm tunable laser source is used to excite resonator modes. The laser is scanned repeatedly through a scan range of 60 GHz, containing a doublet structure while simultaneously recording transmission ($T=|t/s|^2$) and reflection ($R=|r/s|^2$) through the tapered fiber. A typical spectrum is shown in figure 11. By repeating such measurements many times for varying taper-sphere gap the complete range of waveguide coupling regimes can be observed. When combined with the coupled-mode model, the system parameters can be extracted. The data in figure 11 are for a 70-μm-diameter sphere (Q of $1.2\cdot10^8$) and the inferred mode coupling is $\Gamma=10$.
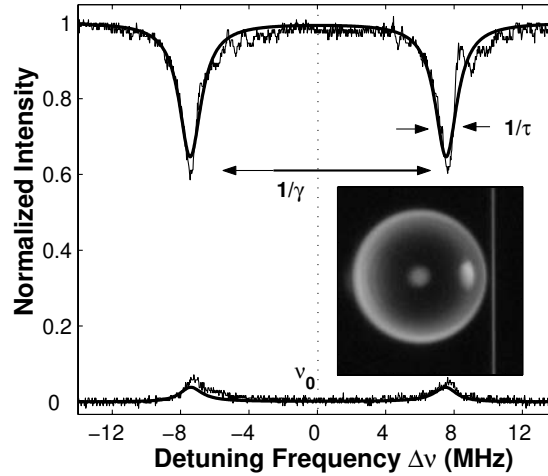

Fig. 11. Transmission and reflection spectra of a 70-μm-diameter sphere with $Q_0=1.2\times10^8$ and modal coupling of $\Gamma=10$. The solid line represents a fit using the coupled-mode equations (eqns.7). The inset shows an optical micrograph of a micro-sphere coupled to a tapered fiber.

Figure 12 contains both data and model curves for transmission and reflection versus coupling measured at a frequency corresponding to the eigen-frequency of the original degenerate modes (ω_0). We refer to this as "symmetric" excitation since it occurs midway between the doublets in the spectrum. In the absence of modal coupling the transmission vanishes (with zero reflection) at the conventional critical point K=1 (waveguide loss and coupling loss are balanced). For comparison with data, the corresponding curve for this case is the dash-dot

curve. Critical coupling also coincides in the case of no modal coupling with the point of maximum circulating power.

In the presence of modal coupling, critical coupling, as defined by vanishing waveguide transmission T=0, can still be achieved, however only for symmetric excitation $\Delta\omega$ =0. The transmission and reflection for $\Delta\omega$ =0 are given by the expressions:

$$T = \left[\frac{\Gamma^2 + (1-K)(1+K)}{\Gamma^2 + (1+K)^2} \right]^2 \; , \quad R = \left[\frac{2 \cdot \Gamma \cdot K}{\Gamma^2 + (1+K)^2} \right]^2 \tag{11}$$

It can be shown that the waveguide transmission vanishes identically for:

$$K \equiv \left(\frac{\tau_{EX}}{\tau_0} \right)^{-1} = \sqrt{1+\Gamma^2} \tag{12}$$

The critical coupling point is therefore strongly dependent on the modal coupling and occurs in what would, under normal circumstances, be considered the over-coupled regime (i.e. for $\tau_{ex} < \tau_0$). The amount of over-coupling required for zero transmission increases monotonically versus modal coupling. (As an aside, we note that the condition K=1 has the special property of causing a transmission and reflection of equal magnitude regardless of inter-mode coupling strength.)
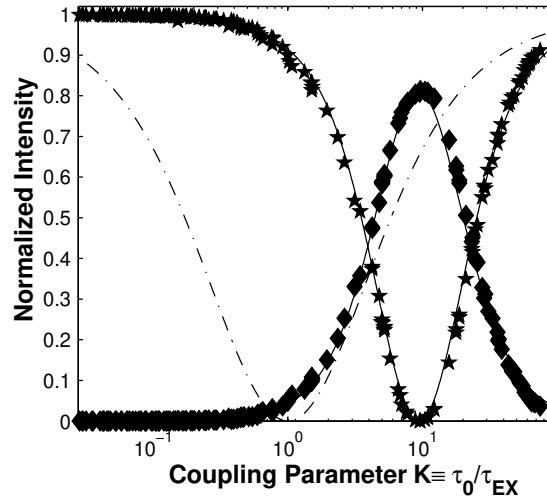

Fig. 12. Transmission (stars) and reflection (diamonds) measured for the case of symmetric ($\Delta\omega$=0) excitation vs. K. Q_0=1.2·10^8 and a modal coupling of Γ=10 are inferred from the data. The solid lines provide a theoretical fit using the mode coupling model from equations 7. The critical point (T=0) occurs at $K_{crit} = \sqrt{1+\Gamma^2}$ and is shifted with respect to the case of zero modal coupling. In

addition the shifted critical point is accompanied by a maximum reflected signal (in this case measured to be 84%). For comparison the dash-dotted curve is the theoretical coupling curve in the absence of modal coupling. The critical point occurs for K=1 in this case.

The shifted critical point also coincides with the point of maximum reflection, which is given by:

$$R_{CRIT} = \left(\frac{\Gamma}{1 + \sqrt{1 + \Gamma^2}} \right)^2 \qquad (13)$$

In the limit of large Γ the reflection approaches unity, and all incoming waveguide power is reflected so that the system behaves as a 'frequency-selective reflector'. We have experimentally verified the above equation as shown in figure 13.
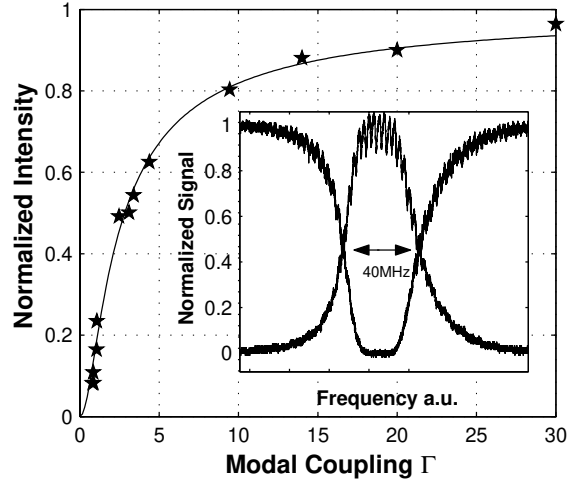

Fig. 13. Stars are the measured maximum reflection as a function of the normalized intermode coupling parameter and the solid line is a theoretical curve using the maximum reflection formula given in the text. The inset shows measured spectral reflection and transmission properties for the case of Γ=30.

The inset shows measured transmission and reflection spectra at the critical point, where the micro-cavity behaves as a frequency selective reflector. These particular spectra were measured using a 30-μm-diameter microsphere exhibiting an inter-mode coupling parameter of Γ=30 (the highest observed in our measurements). This large modal coupling parameter implies a strong likelihood

for photon scattering into the counter-propagating mode versus being lost to numerous other possible mechanisms. We believe this could in part be related to suppression of certain forms of scattering loss by the low angular mode density made possible in the whispering gallery. Only light that is scattered into an angular segment which exceeds the modal cutoff angle is lost; all the remaining scattered power is channeled back into clockwise and counterclockwise propagating WGMs, thereby inducing modal coupling. In agreement with this conjecture, large modal coupling parameters were only found in spheres typically smaller than 40 μm. The origin of strong modal coupling was also investigated by analyzing the sphere's surface with scanning electron microscopy. Spheres exhibiting strong modal coupling were found to contain small, isolated and randomly-distributed contaminants on their surface. These had dimensions of typically hundreds of nanometers. For spheres with negligible mode splitting these structures were absent. The presence of isolated sub-wavelength-scale scattering centers can also be a possible explanation for the occasional observation of asymmetric mode splitting. The standing waves that are present in the regime of strong modal coupling, probe different regions of the sphere's surface, which can lead to different loss rates when scattering is caused by highly localized structures. This, in turn, will cause an asymmetry in the line-shapes of the doublet structure.

As noted above maximum power transfer does not occur at the critical coupling point in the presence of backscattering. On the contrary, it occurs for finite transmission. However, analysis reveals that, unlike the effect backscatter induces in shifting the critical point, the point of maximum power transfer does not significantly change. Indeed, the largest shift occurs for a modal coupling parameter of $\Gamma=1.5$ at which the maximum power transfer point shifts from $K=1$ to $K=1.52$. It is interesting to note that for large modal coupling ($\Gamma\gg1$) the maximum power transfer condition again approaches the condition $K=1$, identical to the condition with no modal coupling ($\Gamma=0$). However, the maximum circulating power in the case of strong modal coupling is reduced by a factor of two with respect to the ideal case, due to the reflection. Figure 14 shows the reduction of circulating power, denoted by $C(\Gamma)$, with respect to the case of no modal coupling as a function Γ. The location of the point of maximum power transfer and the reduction of circulating power will become important in the subsequent sections, when analyzing threshold behavior for nonlinear optical effects.
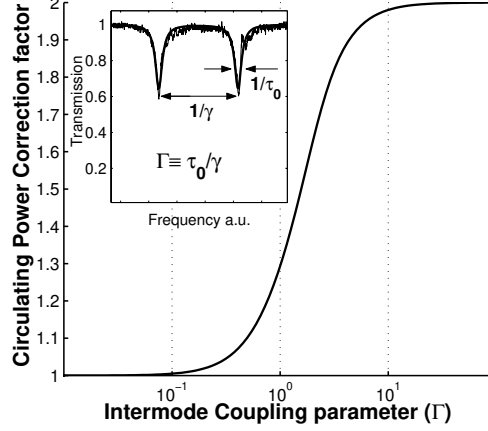
Fig. 14. Reduction of the circulating power (as given by the correction factor C) as a function of the intermode coupling parameter. In the case of strong modal coupling, the circulating power is reduced by a factor of 2 due to coupling of the resonant cavity field along both directions of the tapered fibers.

4.   Mode structure and Q-factors of toroid micro-cavities on-a-chip

4.1. Q-factors of micro-toroids

The Q-factor of the micro-toroid modes were characterized using two different techniques. First, we performed line-width measurements by scanning a single frequency laser through the resonances in the undercoupled regime. The wavelengths measured were in the 1550 nm band. The ultra-high-Q modes typically exhibited a doublet structure and the scans were fit to the coupled-mode model of the previous section and the intrinsic lifetime inferred. The narrowest UHQ linewidths measured are in fact comparable to the short-term linewidth of the external cavity laser used in these measurements (300 kHz short term linewidth). For this reason, as both an independent and more precise means to measure line-width, we also measured the Q-factor by cavity ring-down [18]. In this technique, the laser was scanned successively through a frequency interval containing the resonance to be measured. The scan rate was adjusted to be slow on the timescale of the mode-lifetime so as to prevent line-width distortion due to transient effects. The taper coupling strength was adjusted to the critical point. As the laser progressively scanned, the mode was excited until, at a point near the line center at critical coupling (measurable by setting a trigger level using the

detected reflected power), a high-speed Mach-Zehnder-type amplitude modulator was used to 'gate off' the input laser. With the input laser signal extinguished, the only detectable signal is due to the cavity leakage field which then decays exponentially with a time constant that gives the loaded Q factor for the mode at the critical point. Figure 15 shows a typical experimental trace in the ring-down measurement. At the time t=0 the laser field is gated off and an exponentially decaying field, as is expected for a single mode, can be observed. The deviation of the transmission from unity at t=0 is due to the gating fall time (approximately 8 ns). The inset of figure 15 shows the signal on a logarithmic plot to infer the lifetime and to confirm the single-exponential behavior of the decay signal. A fit to the data in the figure yields an intrinsic lifetime of 75 ns.
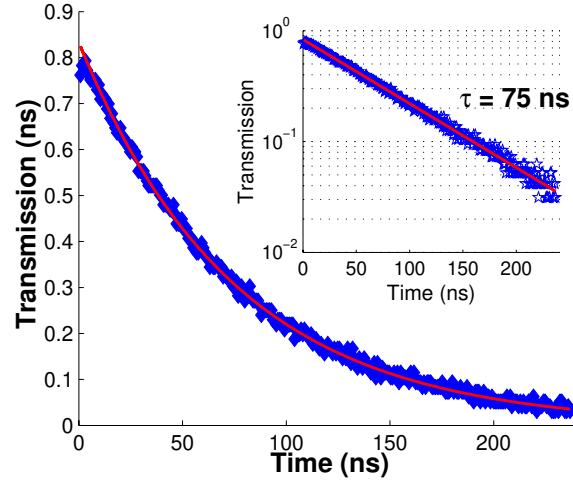

Fig. 15. Cavity ring-down measurement of a micro-toroid cavity mode. At the time t=0 the mode is fully charged at the critical point and the laser is gated off. The inset shows the log-scale plot of the data confirming the single exponential decay.

As noted above, this value corresponds to a loaded cavity Q. To infer the intrinsic Q from this measurement one must take into account the waveguide loading. For an ideal traveling-wave WGM the lifetime at the critical point is precisely half of the intrinsic lifetime. However, as noted earlier, in the UHQ regime the WGMs are typically split into doublets due to weak backscattering. From the previous section, the critical point in the presence of intermode coupling occurs in what would (under zero-backscatter conditions) be referred to as the over-coupled regime. As a result, the actual intrinsic cavity Q is related to the critical-point lifetime by the expression:

$$Q_0 = \omega\tau_0 = \omega\tau_{crit}(1 + \sqrt{1 + \Gamma^2})$$
(14)

The Γ factor can be measured as described in the previous section by measuring the normalized splitting in the under-coupled regime. For the ring-down shown in figure 15, a modal coupling of $\Gamma \approx 3.7$ was present yielding an intrinsic cavity Q of 4.3×10^8.

Generally, thermal effects are present in UHQ silica devices and induce distortion of the lineshape unless input power levels are adjusted to a suitably low value. These distortions tend to make the apparent linewidth larger (pull the center frequency of the mode) in one scan direction while making its appearance narrower in the opposing scan direction. These artifacts present another challenge to Q measurement based upon linewidth measurement alone.

Finally, there is an alternate method for determining the intrinsic Q factor in cases where there is strong intermode coupling induced by backscatter. This approach does not require knowledge of Γ, but rather only the doublet splitting frequency (γ^{-1}). As before, the ring-down lifetime at the critical coupling condition is measured. However, now the following expression is used to relate both this information and the measured splitting frequency to the intrinsic Q factor.

$$Q_0 = \omega \tau_0 = \omega \frac{2}{\tau_{crit}} \left(\frac{1}{\tau_{crit}^2} - \frac{1}{\gamma^2} \right)^{-1} \tag{15}$$

This method is less sensitive to thermal effects since the splitting frequency has been observed to be nearly immune to thermal shifts (assuming that each mode is affected nearly equally by the excitation wave[41]).

In our work we have measured Q factors as high as 500 million in micro-toroids and Q-factors as high as 2 billion in spheres (measured in the 1550 nm wavelength band). While the intrinsic absorption of silica at 1550 nm in principle allows for Q factors of up to 10^{12}, water adsorption and surface scattering losses limit the observed Q to much lower values. Previous studies on micro-spheres [44, 45], have identified water adsorption on the surface as a major limiting factor of the Q. Adsorption of OH molecules has been observed to occur within minutes after the fabrication procedure. The Q-factors in the present work are also believed to be limited by a combination of surface adsorption of OH groups and surface scattering centers on the micro-cavity. Since all measurements reported here were performed in ambient conditions and after a time interval exceeding 5 minutes after micro-toroid fabrication, water adsorption is likely to affect the Q as described in reference [1].

Finally, dielectric microcavities do not, in fact, provide strict confinement of modes as WGMs are always subject to tunnel leakage into the continuum

(sometimes called whispering gallery loss). This leakage rate is primarily a function of the dielectric index-of-refraction as well as the diameter of the WGM orbit. Intuitively, this loss is like the bending loss in a dielectric waveguide. For microspheres the whispering gallery loss has been calculated using asymptotic expansions [46]. In silica spheres having Q values of 100 million in the 1550 nm band, this loss becomes a determining factor in degrading Q for radii less than 11 μm [26]. To investigate the influence of radiation loss on micro-toroids we have measured the Q-factor as a function of the principal micro-toroid radius. The toroid minor radius was approximately constant in this experiment (ca. 8-10 μm). Figure 16 shows the result of this study.
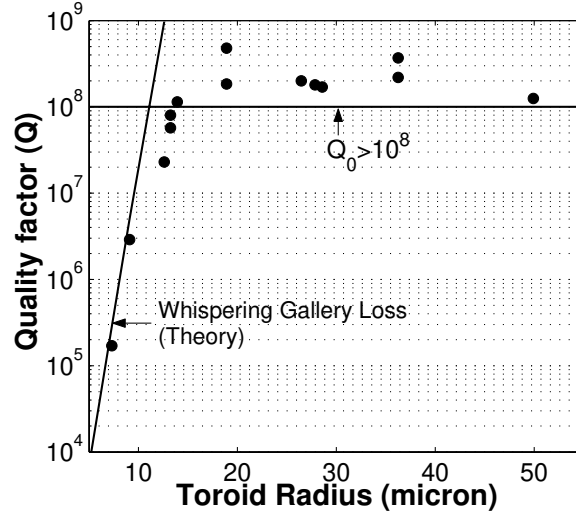

Fig. 16. Measured quality factor of microtoroids as a function of principal radii. For radii smaller than 15 μm the Q factor decreases below 10^8 due to radiation loss. The solid vertical line represents the tunnel loss for the case of spherical whispering gallery modes. The horizontal solid line is a guide to the eye set at a Q value of 100 million.

The results indicate that whispering gallery loss is negligible for principal tori-radii of more than 15 μm. Below this value the Q-factors are seen to decrease as a function of radius and to approach the theoretically calculated limit of whispering gallery loss for a sphere. In addition we have varied the minor toroid diameter to a range of ca. 4 wavelengths (~3.8 μm) and measured Q values of more than 10^8.

4.2. Mode structure of a toroid micro-cavity

Figure 17 is a typical transmission spectrum for a taper coupled to a toroidal micro-cavity. The observed free spectral range corresponds to the modes with successive equatorial (or angular) mode number (ℓ). Successive ℓ-modes exhibit varying amounts of coupling. Inspection of the mode structure shows that the micro-toroid supports only very few transverse and radial modes. This is in contrast to micro-spheres, where each angular mode exhibits a $(2\ell+1)$-fold degeneracy in the azimuthal direction. The number of transverse modes is expected to be a strong function of the toroid rim thickness (minor diameter).
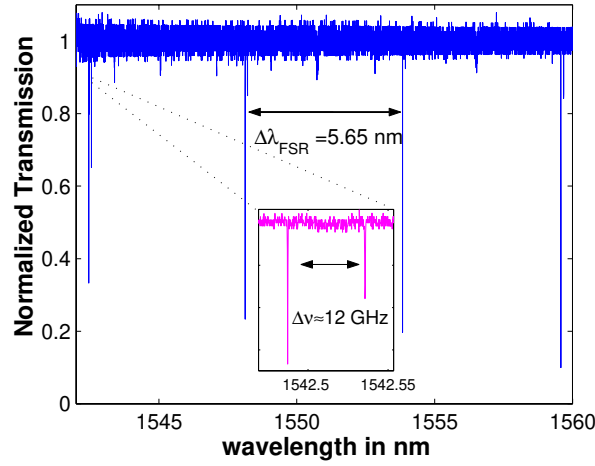

Fig. 17. Transmission spectrum of a toroid micro-cavity of 94-μm-diameter. Successive modes are separated by the free spectral range of the cavity.

Whereas the mode structure of micro-spheres is well known and analytical expressions for the field distribution can be derived, analytical expressions for the toroid geometry are not available as only one coordinate of the wave equation separates, reducing it to a two-dimensional Helmholtz equation. In order to determine the modes of a toroidal micro-cavity, a finite element eigenmode solver was used to model the 2D cross-sectional geometry after accounting for the rotational symmetry. A full-vectorial method was used which allowed accurate solution of the complete field distribution, confirmed for accuracy using the resonance locations and field profiles of a spherical cavity[47]. Figure 18 shows a representative intensity profile for the fundamental TE mode of a toroid micro-cavity with a 6 μm minor diameter (principle diameter of 50 μm),

compared with that of a micro-sphere of diameter 50 μm. For comparison, the first higher-order transverse modes are also shown. While degenerate in a perfect micro-sphere, in this toroid the closest transverse mode is now located 4.6 nm away (approximately half of the free-spectral-range for this principal diameter). This breaking of the azimuthal degeneracy can have a significant effect on the optical properties of these cavities, as discussed in more detail in section 5. Further numerical investigation of toroidal modes indicates a number of additional advantages over spherical cavities, including a more regular free-spectral-range, and a decreased modal volume.
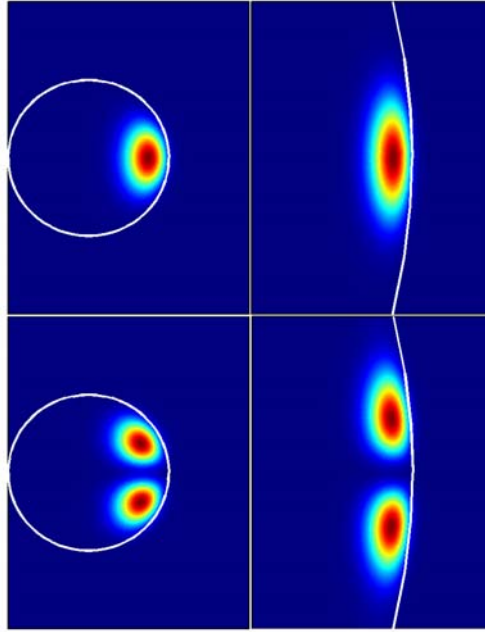

Fig. 18. Intensity profiles for: (left) a toroid (6 μm minor diameter; 50 μm principal diameter) and (right) a micro-sphere with principal diameter of 50 μm. Wavelength is assumed to be near 1550 nm. Both the fundamental (top) and first higher-order transverse modes (TE polarization) are shown in each case.

4. 3. Mode volume of a toroid micro-cavity

In addition to Q, mode volume has a nearly universal influence on micro-cavity performance across a wide range of applications[5]. The mode volume is commonly defined by the spatial integral over the field intensity, normalized to

unity at the field maximum[48]. In the case of spherical micro-cavities the mode volume is readily calculated in terms of the known analytic field distributions. Fundamental-WGM mode volume on the order of 1000 μm^3 is typical for sphere diameters in the range of 100 μm and varies to a good approximation quadratically with sphere diameter over a wide range of values. We have investigated the mode volume of toroidal-micro-cavities using numerical modeling as described above. Figure 19 shows the calculated mode volume vs. toroid minor diameter assuming a 50-μm toroid principal diameter and a fundamental WGM near 1570 nm. Note that the case of unity aspect ratio (minor diameter of 50 μm) corresponds to a spherical microcavity. Therefore the plot also provides the extent of mode volume reduction in a toroid relative to a spherical micro-cavity having the same (principal) diameter.
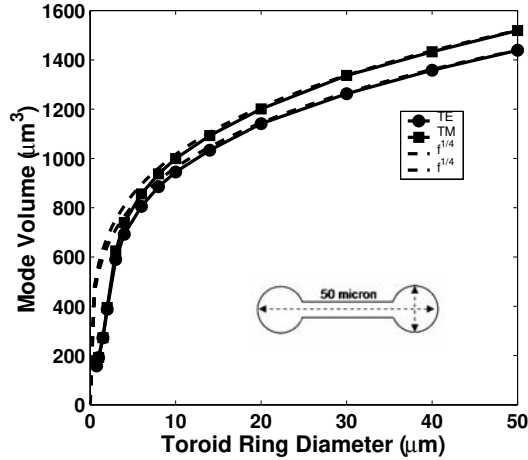
Fig. 19. The mode volume of a fundamental toroidal WGM as a function of minor diameter for 50-μm principal diameter. Results are presented for TE (circles) and TM (squares) modes for a mode near 1570 nm. The dashed lines correspond to a fit using a weak confinement approximation described in the text.

From the numerical modeling it is apparent that one can distinguish between both a slow and fast regime of mode-volume reduction (or compression) with decreasing toroid minor diameter. In the slow compression regime the minor diameter is much larger than the transverse extent of the mode. A simple analysis of the wave equation reveals that in this case an effective harmonic oscillator potential (in theta) associated with the toroidal curvature determines the transverse extent of the mode in the vicinity of the equator. This mechanism is well known in a sphere [26]. In the limit of this approximation, the mode volume

compression relative to the sphere should scale as the $1/4^{th}$ power of the minor to major diameter. This functional form, as indicated in figure 19, is in excellent agreement with the exact calculation over the slow compression regime. A continued reduction then leads to the strong modal compression regime, where the toroid exerts greater influence on the mode volume as the dielectric boundary approaches and closes in upon the mode. Mode volume is reduced until the point where the toroid geometry and associated modes approach those of a step-index fiber. In analogy with a step-index fiber, further reduction of the core area leads to a point where the mode volume is minimal and additional reduction of the minor diameter is accompanied by a decreased mode confinement and increase in mode volume. As described below, we have confirmed the reduction of mode volume experimentally by using the threshold of stimulated Raman scattering to experimentally infer the cavity mode volume.

5 Observation of Nonlinear Oscillations in Ultra-high-Q silica microcavities

Ultra-high-Q micro-cavity modes are ideally suited to study stimulated and parametric optical nonlinear processes. The micro-cavity concentrates input power at resonant frequencies by re-circulating it within a small modal volume. Also, by restricting oscillation to resonant frequencies, it can suppress the occurrence of certain nonlinearities unless specific conditions are satisfied. Nonlinear optics in liquid micro-droplets has been pioneered by Campillo [13] and Chang [10] and an extensive discussion on this topic can be found in reference [4]. Despite their unique properties (UHQ and small modal volume) micro-droplets have remained a laboratory tool, due to their transient nature which makes stable and long term study difficult. In this section we present our results concerning cavity nonlinear optics in UHQ micro-sphere and micro-toroid resonators. These micro-cavity geometries allow stable observation of nonlinear effects and in addition are compatible with fiber-optic technology, as shown in figure 20.

The combination of UHQ and efficient fiber-taper coupling allows the observation of stimulated Raman scattering at unprecedented threshold powers[8]. that are nearly a factor of 1000 lower than prior work using droplet microcavitiesIn addition to their ultra-low threshold, these devices are, from a practical standpoint, compact, fiber-compatible and exhibit high pump-to-Raman conversion efficiency (more than 45% has been measured). Due to the high conversion efficiency, the Raman mode can also build-up to appreciable intensities and exceed the threshold for higher-order Raman generation, which will be the topic of section 5.2.

   Whereas stimulated Raman scattering is intrinsically phase matched, parametric oscillation due to the silica Kerr nonlinearity, requires strict phase matching conditions to be satisfied. In section 5.3 we show how by controlling the cavity geometry a transition from stimulated to parametric oscillation can be achieved, enabling the first demonstration of a micro-optical parametric oscillator.
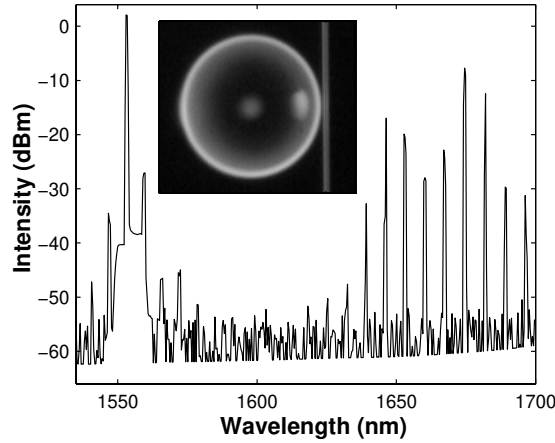

Fig. 20. Nonlinear emission spectrum from a UHQ micro-sphere cavity. The pump is at 1550-nm and the peaks in the 1600 band are due to Raman oscillation. The peaks appearing symmetrically around the pump wavelength are due to Raman-assisted Four-wave-mixing. The inset is a micrograph showing a fiber-taper-coupled microsphere.

5.1 Stimulated Raman Scattering in micro-cavities

   Raman scattering is an inelastic light scattering mechanism [49, 50] in which a photon is converted to a lower energy (Stokes) photon via the emission of an optical phonon. Raman scattering is of considerable technological and scientific importance across a range of topics including spectroscopy, biochemical sensing and quantum optics[51, 52]. Also, due to the broad Raman gain-bandwidth in silica [25] (extending over ca. 10 THz relative to the pump frequency with the maximum gain occurring at a Stokes shift of ca. 14.7 THz or 440 cm^{-1} [53]) optical-fiber-based Raman amplifiers can provide broadband gain in almost any wavelength band [54] and can be employed to extend the wavelength range of amplifiers used in communications systems or semiconductor laser signal sources themselves [55]. There has been extensive research and progress in the demonstration of fiber-Bragg-grating and Fabry-

Perot-type (e.g., those employing gas cells) Raman sources [56]. However, for silica-based devices high pump powers are typically required [55]. In this section we demonstrate the use of STIMs as efficient, compact and ultra-low threshold Raman lasers [8]. Despite the low nonlinearity of silica, these devices exhibit exceptionally low thresholds for Raman oscillation. By adjusting the taper micro-cavity gap we have investigated the influence of coupling on threshold, conversion efficiency and the ability to generate Raman cascades. In particular, the ability to strongly over-couple these cavities enables achievement of very high differential conversion efficiencies.

Before describing experimental results, a review of the essential physics governing Raman lasers will be presented. Raman scattering in a waveguide-coupled UHQ micro-cavity can be described using the coupled-mode equations shown below with nonlinear Raman terms [24] coupling the pump and subsequent Raman orders. Other nonlinear terms associated with processes such as Brillouin scattering or the Kerr nonlinearity are not considered, since their presence in a micro-cavity is strongly restricted as discussed at the end of this section.

$$\frac{dE_p}{dt} = -\left(\frac{1}{\tau_0} + \frac{1}{\tau_{ex}}\right)_P E_p - \left(\frac{\omega_p}{\omega_{R1}}\right) g_{R1} |E_{R1}|^2 E_p + \kappa \cdot s$$

$$\frac{dE_{R(N-1)}}{dt} = -\left(\frac{1}{\tau_0} + \frac{1}{\tau_{ex}}\right)_R E_{R(N-1)} + g_{R(N-2)} |E_{RN-2}|^2 E_{R(N-1)} - \left(\frac{\omega_{R1}}{\omega_{R2}}\right) g_{RN} |E_{RN}|^2 E_{R(N-1)} \quad (16)$$

$$\frac{dE_{RN}}{dt} = -\left(\frac{1}{\tau_0} + \frac{1}{\tau_{ex}}\right)_{RN} E_{RN} + g_{RN} |E_{R(N-1)}|^2 E_{RN}$$

In these equations, "E_i" are the amplitudes of the intra-cavity pump and Raman fields and "s" denotes the input from the waveguide, normalized such that input power is the square of the amplitude s, $P_{in} = |s|^2$. The excitation frequency of the pump mode and the resonant Raman modes are given by ω_p and ω_{RN}, respectively, with τ_0 and τ_{ex} giving the intrinsic and external photon lifetime (i.e., decay time into the waveguide), as introduced earlier. The input field "s" is assumed to be resonant with the pump-WGM. The nonlinear Raman terms are expressed by the intra-cavity gain constant g_R which is related to the more commonly used bulk Raman gain coefficient g^{Bulk}_R (in units of m/W[57]) by (*c* is the speed of light in vacuum, and *n* the index of refraction):

$$g_R = C(\Gamma)^{-1} \frac{c^2}{2n^2} \left(\frac{1}{V_{eff}}\right)_R \cdot g^{Bulk}_R \quad (17)$$

In this relation, the reduction of the cavity buildup factor in the presence of backscatter coupling is described by a circulating power correction factor $C(\Gamma)$ as introduced in section 3.2. In silica the bulk maximum Raman gain coefficient is 10^{-13} m/W at a 1000 nm wavelength [58]. The spatial variation of the Raman gain across the mode profile due to the intensity dependence can be accounted for by introducing the effective mode volume [55].

$$V_{eff} = \frac{\int |E_p|^2 dV \int |E_R|^2 dV}{\int |E_p|^2 |E_R|^2 dV} \tag{18}$$

This definition of effective mode volume deviates from the previously introduced energy-density related definition, because it takes into account the spatial overlap of the pump and Raman modes[55]. For the micro-toroid geometry, numerical modeling shows that improved modal confinement leads to a reduced effective mode volume, in comparison to a spherical microcavity

The threshold for first-order Raman scattering can be derived by considering the steady-state solution to the coupled-mode equations. The threshold formula for first-order Raman scattering can be factorized into contributions of modal volume, coupling dependence (described by coupling parameter K) and the Q factors of the Raman and pump modes.

$$P_{thresh}^{N=1} = C(\Gamma) \frac{\pi^2 n^2}{\lambda_p \lambda_R g_R} V_{eff} \left(\frac{1}{Q_0}\right)_P \left(\frac{1}{Q_0}\right)_R \frac{(1+K_p)^2}{K_p} (1+K_R) \tag{19}$$

The threshold power has an inverse square dependence on the quality factor (assuming equal pump and Raman Q factors) and scales linearly with mode volume. Under the assumption of equal Raman and Pump quality factors, the minimum threshold occurs for K=1/2 (equivalently $Q_{ex}=2 \cdot Q_0$), which corresponds to an under-coupled pump with a waveguide transmission of T=1/9 (or approximately 11%).

We have experimentally verified the dependence of the threshold on the coupling strength. Figure 21 shows the Raman threshold measured for various taper to sphere coupling gaps using a 40-μm-diameter micro-sphere excited at 1550 nm. The minimum threshold for this micro-sphere was 62 μWatts and occurs for a gap shifted from the critical point by 0.15 μm into the under-coupled regime (the zero position in the figure 21 corresponds to the pump-wave critical point). The residual pump transmission at this point was measured to be 12%, in good agreement with the theoretically predicted value of 11%. The observed threshold value is in excellent agreement with the predicted value using the experimentally determined parameters $\Gamma=3$, R=40 μm, and Q=10^8. Figure 22

shows the Raman emission in the 1650-nm band for oscillation on a single longitudinal (i.e., equatorial or ℓ) mode. Higher-resolution inspection of the emission peak revealed that 3-5 azimuthal modes (m modes) were lasing simultaneously (upper inset of figure 22).
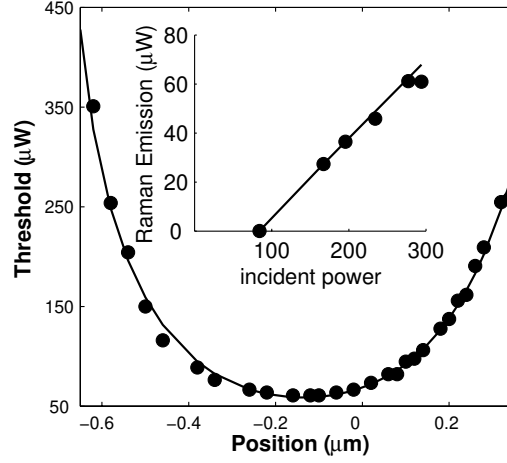

Fig. 21. Threshold for stimulated Raman lasing in a 40-μm-diameter sphere ($Q_0 = 10^8$) as a function of taper-micro-cavity gap with respect to the pump critical-coupling point. The minimum threshold occurs in the under-coupled regime with 12% pump transmission in close agreement with theory. The inset shows the Pump to Raman conversion, exhibiting a bidirectional conversion efficiency of approximately 36% at minimum threshold.
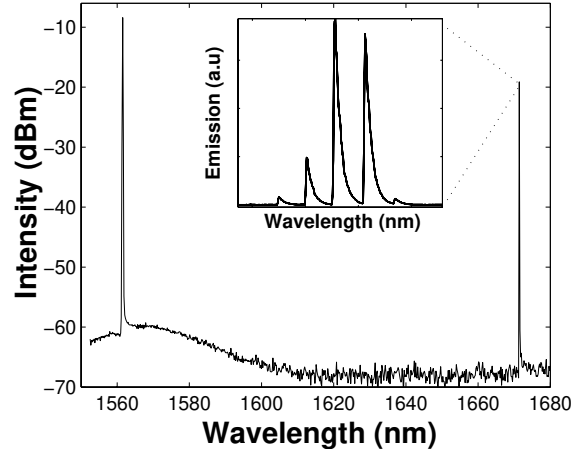

Fig. 22. Single, longitudinal (i.e. equatorial) mode Raman lasing for a micro-sphere of 40 μm diameter. The threshold was measured to be 90 micro-Watts. The inset provides a higher resolution scan and shows that 3-5 azimuthal WGM modes were simultaneously lasing.

Using the coupled-mode equations, the total, first-order Raman output power (which is coupled equally into forward and backward directions of the propagating taper mode) is given by:

$$P_{Raman} = 4 \frac{\omega_R}{\omega_P} \left(1 + \frac{\tau_{ex}}{\tau_0}\right)^{-2} P_{thresh} \left(\sqrt{\frac{P}{P_{thresh}}} - 1\right) \tag{20}$$

It is interesting to note that the 1st order Raman output power follows a square-root behavior with launched pump power, as opposed to being linear. The physical origin of this behavior can be viewed as a "pumping inefficiency" resulting from the dependence of Raman gain on the internal pump wave. This effect can be illustrated by considering operation at the critical point, where the cavity leakage field interferes destructively with the transmitted pump field, causing zero transmission. However, once the onset of Raman lasing is reached, the cavity pump field is clamped at the threshold value and a subsequent increase of pump power will imbalance transmitted pump and cavity leakage fields, giving rise to a finite pump transmission. This "pumping inefficiency" causes the pump power coupled to the cavity to follow the above square-root-behavior on launched fiber power. As the Raman power scales linearly with coupled cavity power, the Raman emission also exhibits a square root behavior on pump power, resulting in the behavior of eqs. 20. We have experimentally confirmed this dependence as shown in the next section (figure 28). For large pump power the first order Raman output saturates due to the presence of higher-order Raman scattering and will be discussed in the next section.

The bidirectional *external* differential pump-to-Raman conversion efficiency is given by linearizing eqn. 20. at threshold:

$$\eta_{ex} = 2 \cdot \frac{\omega_R}{\omega_P} \left(1 + \frac{\tau_{ex}}{\tau_0}\right)^{-2} \tag{21}$$

Figure 23 plots this efficiency as a function of coupling strength. At the point of minimum threshold (K=1/2 assuming equal pump and Raman Q factors) the expected efficiency is 22%. It is 50% at the critical coupling point. The actual measured value in the experiment shown in figure 21 was 36%, which is slightly higher than the theoretically expected value, believed to be due to differences in pump and Raman Q, and due to the presence of modal coupling. The external differential efficiency approaches the value of $2\omega_r/\omega_p$ in the limit of strong over-coupling (i.e., $\tau_0/\tau_{ex}=\infty$). Surprisingly, this value exceeds unity, indicating

that on average every added waveguide pump photon above threshold is converted to more than one Raman photon. This result might seem non-physical, but can be explained when considering the nonlinear dependence of coupled pump power. As the loading experienced by the intra-cavity pump wave is dependent upon the Raman wave once threshold is reached (i.e., the intra-cavity pump field is clamped above threshold), a differential increase in waveguide pump will cause improved coupling to the resonator when the resonator and waveguide are over-coupled. This occurs since the additional loading induced by the, now higher-power, Raman wave shifts the pump wave closer to the critical point. As described above, the opposite effect occurs in the under-coupled regime. This nonlinear loading effect leads to the interesting phenomenon, that the external differential quantum efficiency can exceed unity. In contrast, when analyzing the *internal* pump-to-Raman differential conversion efficiency (i.e. actual-coupled pump to Raman efficiency) one obtains the expression:

$$\eta_{\text{int}} = \frac{\omega_R}{\omega_P}\left(\frac{\tau_0}{\tau_{ex}}\right)\left(1 + \frac{\tau_0}{\tau_{ex}}\right)^{-1} \tag{22}$$

As expected, the internal conversion efficiency approaches the value ($\omega_r/\omega_p < 1$) in the limit of strong overcoupling. This quantity is also plotted versus waveguide-resonator coupling in figure 23.
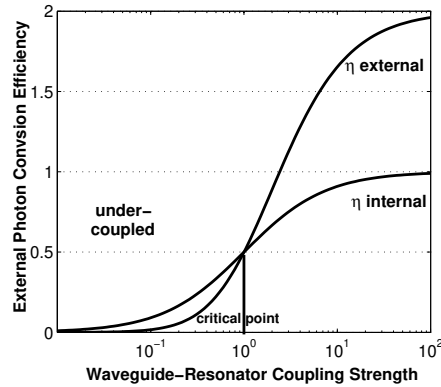

Fig. 23. Internal and external pump-to-Raman differential quantum efficiency as a function of waveguide coupling. The internal and external efficiency are equal at the critical coupling point. In the limit of strong over-coupling the internal efficiency approaches unity, whereas the external efficiency approaches 2.

As noted above, the threshold scales linearly with the modal volume. The mode volume of a silica micro-sphere WGM scales approximately quadratically

with radius As an aside, for smaller spheres the mode volume deviates from this behavior and ultimately, for very small diameters, increases due to weakening of the whispering gallery confinement[46]. The minimum mode volume occurs for a diameter of 6.9μm (for l=m=34) [46] for 1550 nm wavelength (mode volume is V=173.1μm³). However, this size is not optimum for stimulated Raman scattering as the additional benefit of reduced mode volume is more than offset by the significant decrease in Q factor to 10^8 [26](Note: threshold power scales like $\propto Q^2/V$).

We have investigated the dependence of the Raman threshold on mode volume by varying the micro-sphere radius. To enable comparison of micro-spheres with varying quality factor Q, modal coupling parameter Γ and Raman and pump wavelength, we have normalized the threshold values using the dependences appearing in the threshold formula. Furthermore, the Q factors of pump and Raman waves are assumed equal. The result of this study is presented in figure 24. In micro-spheres of less than ca. 25 μm diameter, stimulated Raman scattering was not observed, since thermal drifting effects make pumping of the modes unstable and the whispering-gallery loss becomes a significant loss mechanism [26]. The normalized threshold indeed exhibits a quadratic dependence (actual inferred exponent was 1.93) on micro-sphere radius and is in excellent agreement with the theoretical predictions ($\propto R^{1.83}$) for micro-spheres in this size range[46].
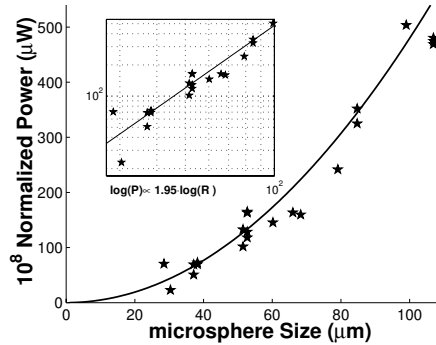

Fig. 24. Normalized Raman threshold vs. sphere diameter. The inset shows a linear fit to a double logarithmic plot to infer the exponent (i.e. $V \propto R^n$), which is n=1.93 and in good agreement with the theoretically expected value of n=1.83 for this range of sphere sizes.

In previous work on micro-droplets it has been found that the Raman gain coefficient inside a micro-cavity experiences a further enhancement due to the presence of cavity-QED effects[12, 13, 59]. For the size ranges measured in this work, our experimental data does not reveal such an effect, and the bulk Raman

gain yielded good experimental agreement. This is also confirmed by recent theoretical work[60].

Other nonlinear effects such as stimulated Brillouin scattering and Four-wave mixing exhibit gain constants that exceed the Raman gain[57]. However, in the above experiments stimulated Brillioun scattering was not observed and four-wave mixing occurred only in certain cases (as a Raman assisted process). Despite the larger nonlinear gain coefficient of Brillouin [54] scattering (by a factor of 500 compared to Raman), the narrow Brillouin gain bandwidth (ca. 100 MHz) poses strong restrictions on the occurrence of this process in a micro-cavity due to the necessity of doubly resonant cavity modes (pump and Raman). The process is particularly restricted in toroid micro-cavities due to the low density of modes. Likewise, the additional condition of phase-matching imposes strong restrictions on the observation of parametric oscillations due to the Kerr nonlinearity. We will turn to the observation of this interesting nonlinear process in section 5.4[61]. Finally, we note that the power levels for catastrophic self focusing [62, 63] are far beyond the intensity levels used in the work presented here.

5.2. Cascaded Stimulated Raman Scattering in micro-cavities

The high internal Raman conversion efficiency within the micro-cavity allows the Raman mode to reach power levels sufficient for pumping a subsequent Raman laser within the same micro-resonator (i.e., cascaded oscillation). This higher-order process is easily observable as shown in figure 25, which shows a second-order cascade.
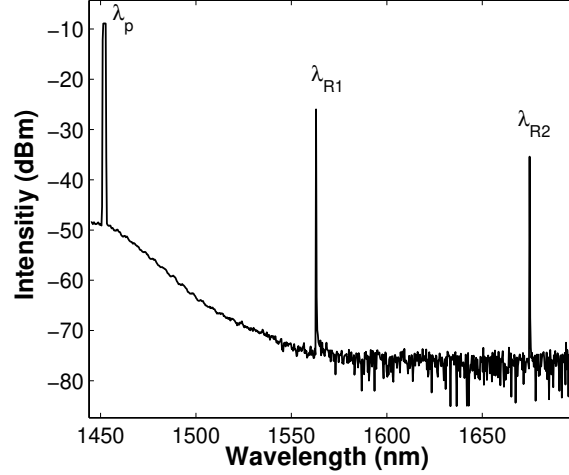
Fig. 25. Cascaded Raman lasing in a 56-μm diameter micro-sphere. The pump is located at 1450 nm and the first and second order Stokes waves are present around 1580 and 1660 nm.

This cascade process can be described by extending the previously introduced model to include higher-order Raman terms. The equations can be solved iteratively in steady state, where we have made again the simplifying assumption of equal pump and Raman Q as well as equal pump and Raman coupling properties. The corresponding pump threshold power given below takes on two distinct forms depending upon whether the Raman order is even ($N = 2m$) or odd ($N = 2m+1$).

$$P_t^{N=2m} = \frac{fC(\Gamma)\pi^2 \text{n}^2}{\lambda_p \lambda_R \text{g}_R} \text{V}_{\text{eff}} \left(\frac{1}{Q_0}\right)^2 \cdot \left(\sum_{i=0}^{m-1}(c_i)^i\right)\left(\sum_{i=0}^{m}(c_i)^i\right)^2$$

$$P_t^{N=2m+1} = \frac{fC(\Gamma)\pi^2 \text{n}^2}{\lambda_p \lambda_R \text{g}_R} \text{V}_{\text{eff}} \left(\frac{1}{Q_0}\right)^2 \cdot \left(\sum_{i=0}^{m}(c_i)^i\right)^3$$

(23)

The coefficient c_i is defined as:

$$c_i \equiv \frac{\omega_i}{\omega_{i+1}} \cdot \frac{g_{i+1}}{g_{i+2}} = \frac{\omega_i}{\omega_{i+2}} \cdot \frac{V_{eff}(\lambda_{i+2})}{V_{eff}(\lambda i)}$$

(24)

where the Raman gain coefficient[57] dependence has been used in the second equality. For stimulated Raman scattering in silica at optical frequencies the Raman shift is generally small compared to the frequency of the light so that the

coefficient $c_i \approx 1$. In addition it has been assumed that the mode volume is independent of wavelength.

Analysis also shows that even and odd-ordered Raman modes have different pump-to-Raman conversion characteristics. The corresponding Raman output powers for even or odd highest orders are given by the expressions:

$$P^{N=2m+1} = \eta_{ex}^N 2\left(\sqrt{P_t^N P} - P_t^N \right)$$
$$P^{N=2m} = \eta_{ex}^N \left(P - P_t^N \right)$$

(25)

Furthermore, when the highest-order Raman line is of odd-order all even order modes are clamped and vice versa. Therefore, for odd, highest order, all odd-ordered Stokes modes exhibit a square-root dependence on pump power with even orders clamped; whereas for even, highest order, all odd ordered modes are clamped and even orders increase linearly with pump power. This characteristic is shown graphically in figure 26. The corresponding external differential conversion efficiencies are given by the expressions:

$$\eta_{ex}^{N=2m+1} = \frac{\lambda_p}{\lambda_{RN}} \left(1 + K^{-1} \right)^{-2} \frac{8}{(N+1)^2}$$
$$\eta_{ex}^{N=2m} = \frac{\lambda_p}{\lambda_{RN}} \left(1 + K^{-1} \right)^{-2} \frac{16}{(N+2)^2}$$

(26)

The conversion efficiencies decrease monotonically vs. Stokes order and for large values of N follow a $1/N^2$ dependence.
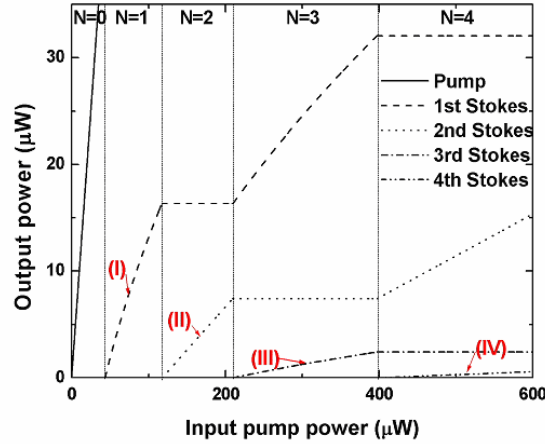
Fig. 26. Pump to Raman conversion characteristic for first and higher-order cascaded Raman modes. The highest Stokes order is denoted at the top of each region. When not clamped, even-order lines increase linearly and odd-order lines increase as the square root with launched pump power.

From expression (23) it can be inferred that for higher-orders the Raman threshold exhibits an approximate cubic scaling with order ($\propto N^3$):

$$P_t^{N=2m} = \frac{fC(\Gamma)\pi^2 n^2}{\lambda_p \lambda_R g_R} V_{eff} \left(\frac{1}{Q_0}\right)^2 \cdot \frac{(1+K)^3}{K} \cdot \frac{(N+1)^3}{8}$$

$$P_t^{N=2m+1} = \frac{fC(\Gamma)\pi^2 n^2}{\lambda_p \lambda_R g_R} V_{eff} \left(\frac{1}{Q_0}\right)^2 \cdot \frac{(1+K)^3}{K} \cdot \frac{N(N+2)^2}{8}$$

(27)

   To verify these theoretically predicted behaviors we have measured stimulated Raman scattering in micro-spheres up to fifth order [24]. The experiments were carried out using pump wavelengths in the 980-nm and 1550-nm bands. Figure 27 contains a spectrum taken using a 980-nm-pump wave. The spectrum contains five distinct orders, each of which contains several oscillating modes. Figure 28 shows the Raman output power for the highest order Stokes wave for cases in which up to four orders are present [24]. The predicted linear and square root behavior of Stokes power with pump power is evident. In the upper left panel of this figure, the apparent flattening of the power is a result of the onset of oscillation in a next, higher-order Stokes wave, which causes a clamping of the field.
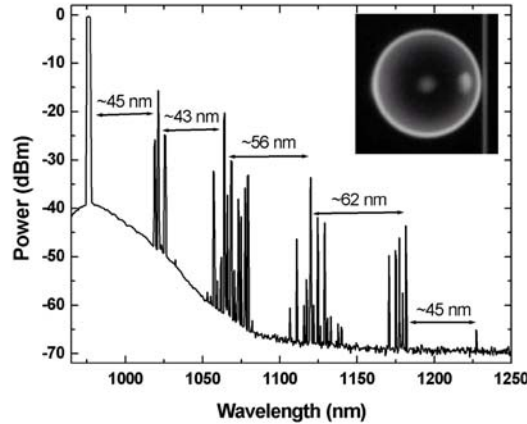

Fig. 27. Emission spectrum of a micro-sphere cascaded Raman laser. The pump wavelength is set to 976 nm and approximate Stokes shifts are specified. Inset: micrograph of a micro-sphere-taper system used in the experiment.
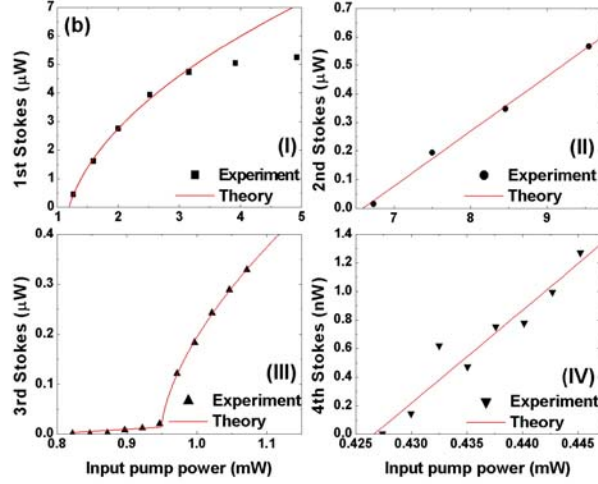
Fig. 28. Stokes lasing powers (1st, 2nd: 1550 nm pumping, 3rd, 4th: 980 nm pumping) versus input pump power. Each data set corresponds to measurements taken using a different micro-sphere.

Theoretical predictions concerning the dependence of threshold and differential conversion efficiency on Stokes order are also in agreement with the measured values as can be seen in figure 29.
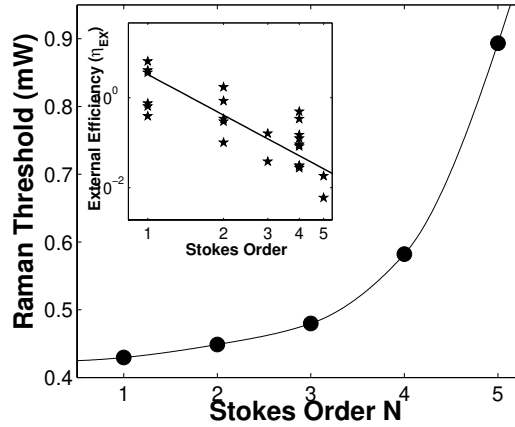

Fig. 29. Measured Raman threshold as a function of Stokes order exhibiting an approximately cubic dependence on Raman emission order. The inset shows the measured conversion efficiency as a function of order, which decreases as predicted by theory (solid line).

5.3. Stimulated Raman scattering in micro-toroids

The experimental results in the previous section concerned stimulated Raman scattering in spheres. The micro-sphere geometry does not, however, allow for single-mode Raman lasing, since the mode structure in the azimuthal direction is nearly degenerate and densely populated with modes (i.e., the m-index modes). As noted earlier, chip-based micro-toroids possess a number of significant and practical advantages when compared to micro-spheres, which includes a reduced mode density due to severe exclusion of azimuthal degrees of freedom. Furthermore, their chip-based nature offers enormous fabrication advantages in terms of process parallelism and the ability to integrate with electrical or optical functions. In this section we use the ultra-high-Q micro-toroids to investigate the performance of the first chip-based micro-Raman lasers. Particular attention is paid to the use of the toroid geometry to achieve reduction of mode volume relative to a micro-sphere and hence a corresponding reduction in Raman threshold.

Figure 30 shows measured fiber-coupled Raman power versus fiber-launched pump power for a micro-toroid-based Raman laser. The device exhibits a differential conversion efficiency of 45%, close to the theoretical prediction for operation at the critical point. Threshold powers as low as 70 μWatts have been measured using these devices. In contrast to micro-spheres, Raman oscillation in micro-toroids was consistently observed to be single mode, due the highly reduced mode spectrum, as shown in the inset of figure 30. This degree of modal purity constitutes a significant improvement over previous reports of nonlinear optical processes in ultra-high-Q micro-cavities and is important for both applied and fundamental applications.
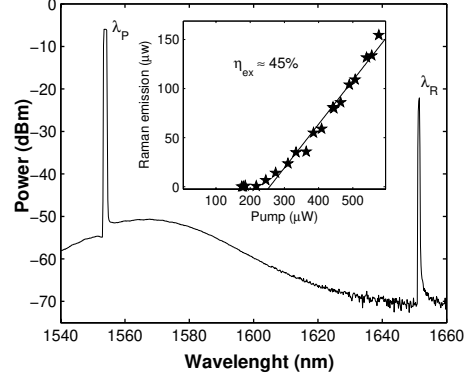
Fig. 30. Raman laser based upon a micro-toroid on-a-chip. The observed emission is single transverse mode. Inset shows Raman emission versus launched pump power. The conversion efficiency was approximately 45% at the critical point, close to the theoretical optimum.

In comparison to micro-spheres, the toroid cavity geometry allows a higher degree of control over the mode volume, as was explained in the section 4.3. In a micro-sphere mode volume can be controlled only by variation of the principal radius, whereas in a toroid the mode volume can be controlled independently using the principal diameter and minor diameter, as shown in figure 31. This has potential advantages in certain applications, such as in nonlinear optical studies, where Q and mode volume must be optimal (i.e. the ratio Q^2/V being maximum). In a micro-sphere, the onset of whispering gallery loss imposes a lower bound on the mode volume for nonlinear wave generation. For Q values in the range of 100 million, this limit corresponds to a sphere diameter of ca. 22 μm at 1550 nm wavelength[26] (at which point the Q becomes radiation loss limited to 100 million). Below this radius any reduction of Raman threshold due to the decreased mode volume is compensated for by increased whispering gallery loss. However, in a toroid of similar size a further reduction of mode volume is allowed by the extra degree of freedom given by the minor toroid diameter. As a result, the performance of a Raman laser on a chip should allow lower thresholds when compared to a comparably sized spherical micro-cavity and for a size range that is not whispering-gallery loss limited.

To investigate the effect of toroid mode volume on Raman threshold, micro-toroids were fabricated with approximately constant principal diameter (in the range of 50-65 μm) and varying minor diameter. For a principal diameter of 55 μm, the onset of the strong mode-volume compression regime (see section 4.3) is predicted to occur near an 8 μm minor diameter. To isolate the effect of mode volume on threshold power, a normalized threshold power was computed in a

manner similar to that used for figure 24 in the case of the spherical cavity. As before, Q factor (as well as backscatter splitting) was measured in the pump band and the assumption of identical pump and Raman band Q factor was applied. Q factors were measured by cavity ringdown. Because of the substantial difference in frequency of neighboring toroid modes, significant variations in Raman gain are possible and were corrected-for by measurement of the pump and Raman wavelengths for each data point and application of the known Raman spectra of silica [25]. The slight variation in the principal toroid diameter was also taken into account by applying a normalization factor resulting from a numerical model. To infer the effective minor diameter we used a scanning electron microscope (SEM) and recorded the cavity side profile. Figure 31 shows a typical side profile of a micro-toroid used in this study. The toroids in most cases exhibit a circular profile, as was confirmed by fitting the SEM profile. However, in some cases a deviation to a more parabolic profile was observed and the effective toroid minor diameter was inferred by curve fitting the equatorial curvature.
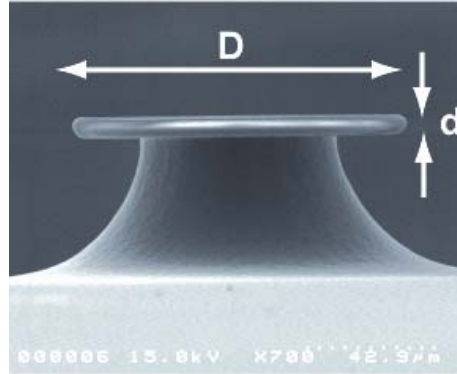
Fig. 31. SEM side profile of a toroid micro-cavity showing the principal and minor toroid diameters.

A plot of the experimentally determined effective volumes is given in figure 32. For comparison the figure also contains data obtained from Raman threshold measurements obtained using a silica sphere of comparable diameter [8] (i.e., equal principal and minor diameter) as well as the numerically predicted dependences of the mode volume for TE and TM polarizations. Variation in the measurement results is most likely due to lack of knowledge of the actual Raman Q factors, however, a good qualitative agreement with the theoretical prediction is obtained.

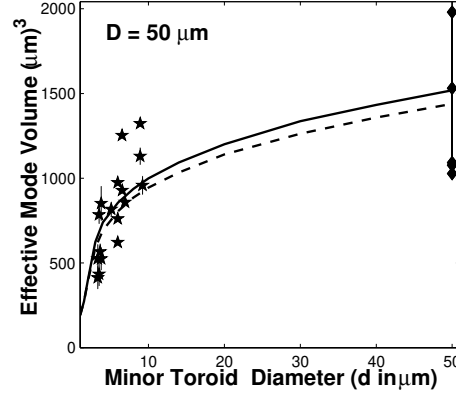Fig. 32. The measured effective mode volume for micro-toroids (stars) and micro-spheres (diamonds) as a function of toroid minor diameter. The curves provide the theoretical dependence. The solid line refers to the TM polarization of a fundamental toroidal WGM, while the dashed line designates the TE polarization case.

5.4. Optical parametric oscillations in toroid micro-cavities

Optical parametric oscillators (OPOs) rely on energy and momentum conserving processes to generate light at new frequencies. In contrast to oscillation based on stimulated gain – e.g. Raman - optical parametric oscillation does not involve coupling to a dissipative reservoir. The lack of such dissipation makes it uniquely suited for fundamental studies, such as the generation of non-classical states [64, 65] for quantum information research [33] as well as in numerous applied areas (e.g. photonics, spectroscopy, sensing). However, oscillation based on parametric gain requires stringent phase matching of the involved optical fields [53]. This combined with the necessity of high field intensity poses severe challenges to attaining micro-scale optical parametric oscillators. In fact, whereas micro-scale stimulated nonlinear oscillators have been demonstrated [4, 8 , 10, 13, 66-68, 69], micro-scale optical parametric equivalents have never been realized. In this section we demonstrate a micro-scale optical parametric oscillator (µOPO) using toroid microcavites.

While ultra-high-Q ensures high circulating field intensities within the resonator [70], causing a variety of nonlinear optical effects [4, 8, 10, 13, 66, 71], it is not a sufficient condition to ensure parametric oscillation. Due to inversion symmetry, the lowest order nonlinearity in silica is the third-order nonlinearity so

that the elemental parametric interaction converts two pump photons (ω_p) into signal (ω_s) and idler (ω_I) photons [53, 65]. In order for parametric oscillations to efficiently occur, both energy and momentum must be conserved in this process [53, 61]. For WGM-type modes momentum is intrinsically conserved when signal and idler angular mode numbers are symmetrically located with respect to the pump mode (i.e. $l_{i,s} = l_p \pm N$). Energy conservation, on the other hand, is not expected to be satisfied a priori, since the resonant frequencies are, in general, irregularly spaced due to both cavity and material dispersion. As a result, the parametric gain is a function of the frequency detuning $\Delta\omega = 2\omega_P - \omega_I - \omega_S$, which effectively gives the degree to which the interaction violates strict energy conservation. It can be shown that the existence of parametric gain requires that this detuning be less than the parametric gain bandwidth [61]

$$\Omega = 4 \cdot \frac{c}{n}\gamma P \text{, and } \gamma = \frac{\omega}{c} \cdot \frac{n_2}{A_{eff}} \tag{28}$$

where is γ the effective nonlinearity, n_2 is the Kerr nonlinearity ($n_2 \approx 2.2 \times 10^{-20} \, m^2/W$ for silica[53]) and P is the circulating power within the micro-cavity. To achieve a cavity detuning within the parametric gain bandwidth i.e. $0 < \Delta\omega < \Omega$ a reduction of the toroidal cross-sectional area will produce a two-fold benefit. First, it increases the parametric bandwidth Ω through its dependence on γ[61], and second, it reduces $\Delta\omega$. The increase of Ω occurs, since a decrease in toroid cross-sectional area will reduce the modal effective area A_{eff} as described in section 4.3. The reduction of $\Delta\omega$ occurs because of increased modal overlap with the surrounding dielectric medium (air) and hence flattening of the modal dispersion. Thus, the desired transition can be induced with toroidal geometries of high principal-to-minor toroid diameter (high aspect ratio).

By equating parametric gain and micro-cavity loss (as given by the loaded cavity Q factor), the necessary launched pump power in the fiber for parametric oscillation threshold is obtained:

$$P_t^{PARAM} = \frac{\omega_0^2 Q_0^{-2}(1+K)^2 + (\Delta\omega/2)^2}{\gamma\Delta\omega} \cdot \left(\frac{\pi^2 R n_{eff}}{2C(\Gamma)\lambda_0} \frac{(K+1)^2}{K} \cdot \frac{1}{Q_0} \right) \tag{29}$$

Here K is again the coupling parameter (as defined in eqn. 10), *R* is the principal cavity radius, n_{eff} is the effective index and C(Γ) is the modal coupling correction factor as shown in fig. 14 of section 3.1. Figure 33 shows both parametric and Raman oscillation regimes as a function of the detuning frequency $\Delta\omega$ and the

coupling parameter K. The threshold pump power for parametric oscillation is color-coded as indicated. As stimulated Raman scattering does not depend on the detuning frequency (i.e. it is intrinsically phase-matched; compare the threshold eqn. 19 in section 5.1), it is the dominant nonlinear mechanism by which light is generated for large detuning values. With decreasing $\Delta\omega$ (or equivalently increasing toroidal aspect ratio D/d), a transition from stimulated to parametric regimes occurs when the threshold for parametric oscillation falls below that for Raman. Also note that for increased waveguide loading (and hence correspondingly higher threshold pump powers) the transition can be made to occur for detuning values that are progressively larger.
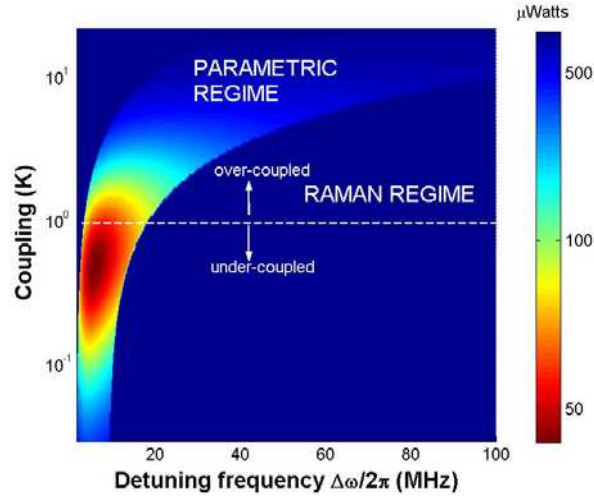

Fig. 33. Nonlinear processes in a toroidal micro-cavity with D=50 μm, d=4 μm and $Q_0=10^8$. The vertical axis denotes coupling strength K of the waveguide-resonator system while the horizontal axis denotes frequency detuning (i.e. $\Delta\omega = 2\omega_P - \omega_I - \omega_S$). The dotted line corresponds to the critical coupling point. The dark blue region denotes areas where Raman oscillation occurs. The color-coded region corresponds to the parametric oscillation regime (where the parametric threshold is indicated by color in micro-Watts).

In order to confirm this prediction, the nonlinear optical properties of toroid micro-cavities with an approximately constant principal diameter ($50\mu m \leq D \leq 70\mu m$) and varying minor diameter (d) were measured. Due to the ultra-high-Q of the toroidal whispering-gallery modes (WGMs), ultra-low-threshold, stimulated Raman scattering was consistently observed for toroids having an aspect ratio of ca. D/d< 15, as described in section5.3.

For micro-toroids having an aspect ratio (D/d) in excess of ca. 15 a transition (and a subsequent quenching of Raman [50, 72]) to parametric oscillation was observed. Figure 34 shows a parametric oscillation emission spectra for a micro-toroid with d=3.9 μm, D=67 μm and $Q_0=0.5\times10^8$. In this measurement a single fundamental WGM of a micro-toroid is pumped in the telecommunication window near 1550-nm using tapered optical fiber waveguides [19, 20]. The parametric interaction in the micro-cavity causes emission of co-propagating signal and idler modes, which are coupled into the forward direction of the tapered fiber. Some residual signal and idler reflection was detected in the backward direction due to the presence of modal coupling, induced by backscattering[21]. The generated signal and idler modes had identical oscillation threshold, within the experimental resolution set primarily by taper coupling variations (ca.±5%).
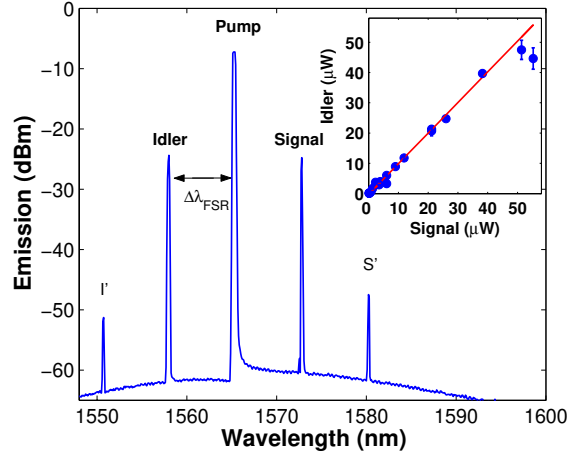
Fig. 34. Parametric-oscillation spectrum measured for a 67-μm–diameter toroidal micro-cavity. The pump is located at 1565 nm and power levels are far above threshold. The signal and idler are modes with successive angular mode numbers and are spaced by twice the free spectral range (2×7.6 nm). The subsidiary peaks (denoted I',S') only appeared at high pump powers and are due to a combination of nonlinear effects, such as parametric oscillation (of signal and idler) as well as four-wave-mixing involving the idler, pump and signal. Inset: idler emission power plotted versus the signal emission power, recorded for different pump powers. The signal-to-idler power ratio is 0.97±0.03. For higher pump powers deviation is observed due to appearance of secondary oscillation peaks (I',S') (compare main figure).

Figure 35 shows the parametric oscillation threshold as a function of taper-toroid coupling gap for the toroid micro-cavity of figure 34. Analysis of the

threshold equation 29 shows that the coupling point of minimum threshold is a function of the detuning frequency. At the optimum frequency detuning (i.e. maximum parametric gain, for $\Delta\omega_{opt} = 3 \cdot \omega \cdot Q^{-1}$), the minimum threshold occurs under-coupled for K=0.5 with finite pump transmission (T=1/9), as was also the case for stimulated Raman scattering considered in section 5.1 (compare with eqn.19 for the SRS case). For larger detuning the minimum threshold point shifts towards being over-coupled (compare figure 33). The measured minimum threshold in the figure was 339 µWatts and occurred for the taper displaced by 0.04 µm into the under-coupled regime. The corresponding pump transmission was T≈4% (K = 0.7), indicating that the frequency detuning is close to being optimum.
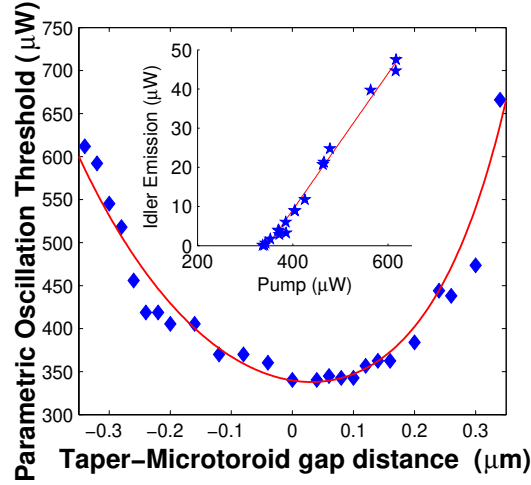
Fig. 35. The coupling-gap-dependence of the parametric threshold with respect to the critical coupling point measured using a 67-µm-diameter toroid micro-cavity. The minimum threshold occurs with the tapered optical fiber 0.04 µm under-coupled (with finite transmission of ca. 4%). The solid line is a theoretical fit using the threshold equation. Inset: Idler emission versus pump power. The differential conversion efficiency from pump-to-idler was ~17% (and correspondingly 34% for pump to signal and idler).

Above threshold the signal and idler fields increase approximately linearly with pump power (for high pump power P, the emission scales $\propto \left(\sqrt{P/P_t} - 1 \right)$ which is due to clamping of the intracavity pump field, as described in section 5.1). The inset of figure 35 shows a pump-to-idler conversion characteristic at the point of minimum threshold. The corresponding external differential conversion

efficiency (compare section 5.1) was 17% pump-to-idler while the total differential conversion efficiency of pump to both signal and idler fields was 34%. Comparison of the conversion efficiency to theory $2\left(1 + K^{-1}\right)^{-2}$ is consistent with the minimum threshold occurring under-coupled, as the inferred coupling point is K≈0.7 (corresponding to T=4% in agreement with the above measured value). Using the minimum threshold data and the cavity ringdown measurements, a detuning frequency of $\Delta\omega/2\pi \approx 24$ MHz is inferred from the threshold equation, compared with $\Delta\omega_{opt}/2\pi = 11.6$ MHz for optimum detuning frequency at the measured Q value. The lowest measured parametric oscillation threshold for the micro-toroids in this study was 170 micro-Watts of launched power in the fiber (for a micro-cavity with D/d=16, d=4 μm, Q_0=1.25×10^8 and $\Delta\omega/2\pi \approx 18$ MHz) and is a factor of 200 lower than for fiber OPOs [73] that utilize the remarkable dispersion control provided by photonic crystal fiber [74].

As a further independent confirmation that indeed the emission can be attributed to parametric oscillation, both signal and idler emission were recorded simultaneously for varying pump power. From theory a signal-to-idler photon creation ratio of unity is expected for parametric oscillation [53]. The inset of figure 34 shows the measured idler emission power plotted versus signal emission power through the optical fiber taper. The measurements were corrected for modal coupling [21] by measuring the reflected power for all three resonances at the critical point, using the procedure described in section 3.1. After correcting for modal coupling, the ratio of signal-to-idler conversion was 0.97±0.03. The observation of near-unity signal-idler emission ratio, combined with the observed identical threshold for signal and idler modes, demonstrates that the observed emission bands can solely be attributed to Kerr-induced micro-cavity parametric oscillation. This observation constitutes the first report of optical parametric oscillation in a microcavity.

In addition to the highly advantageous practical aspects of on-chip micro-cavity nonlinear oscillators, such as wafer-scale integration and control, compact form factor and possible integration with other functions, these oscillators exhibit important properties due to the nature of the underlying nonlinear process within the micro-cavity. Specifically, a phase-sensitive amplification process that can exclude competing Brillouin or Raman processes, as demonstrated here, can provide an excellent candidate system for the generation of non-classical states of light[36, 64, 65, 75-80] on a chip. Whereas the work presented here has used the third order nonlinearity of silica itself, it should also be possible to induce

second-order nonlinear interaction (such as parametric down-conversion), by using ultraviolet[81] or thermal-electric[82] glass poling techniques. This would be important in quantum information[33] and quantum optical studies[65, 83-85] as well as for novel bio-imaging schemes based on entanglement[86].

6. Surface functionalization

In contrast to the intrinsic nonlinear optical properties of silica, the surface of silica STIMs can also be modified to obtain extended optical functionality. This can be achieved in many ways, including ion-beam implantation or spin-coating techniques. In this section a novel sol-gel coating technique is described that enables functionalization of both micro-toroid and micro-sphere cavities with layers of erbium doped silica. When pumped, the resulting devices are efficient lasers (a micro-toroid is illustrated in figure 36 and oscillates in the 1.55-μm-telecom band).

The surface functionalization process begins by dip-coating[87] a chip (or sphere) containing silica microtoroids using erbium-doped sol-gel. The process details are contained in references [88] and [87]. Subsequently, the micro-toroids are selectively annealed using a CO_2 laser, causing the sol-gel films to reflow and densify selectively at the toroid periphery. Owing to the high thermal conductivity of silicon, Sol-gel deposited in regions away from the toroid periphery remains un-densified during this irradiation step, and can be selectively removed in a subsequent hydrofluoric etch step (due to the higher etch rate of non-densified sol-gel films).

The microtoroids functionalized this way will lase in the 1500 nm band when pumped at any of the standard Erbium pump bands [88]. Since high-Q factors can be maintained in this process, low threshold lasing is obtained.
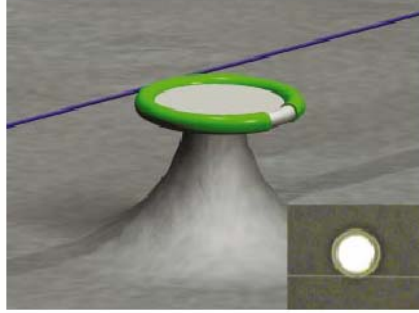
Fig. 36. Illustration showing a silica microtoroid which has been surface functionalized with a thin Erbium sol-gel film. Also shown is a tapered optical fiber for both pump and laser emission extraction.

Figure 37 shows the laser emission in the 1500-nm band as a function of pump power (980 nm wavelength). Extrapolation of the data reveals a threshold of 34 μWatts [88]. Moreover, the emission spectrum was single mode with a differential quantum efficiency of 11%.

Fig. 37. Measured uni-directional laser output power versus absorbed power for an 80-μm-diameter Erbium sol-gel coated microtoroid.

Future work will address alternative routes to optical functionalization using ion-beam implantation.

7. Outlook and Summary

In this chapter we have reviewed the properties of UHQ STIMs including their direct coupling to optical fiber via tapers. This included a review of the coupling

regimes as well the concept of junction ideality. Taper junctions have been shown to be exceptionally low loss and ideal and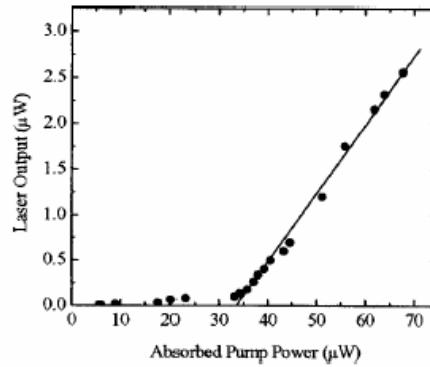 as such are uniquely well suited for certain applications that require ultra-low-loss such as quantum optical studies. The ability to efficiently access UHQ micro-cavity modes using fiber-tapers allows the study of nonlinear optical mechanisms such as the Raman or Kerr nonlinearities and we have described compact, fiber-compatible Raman lasers and Parametric oscillators exhibiting ultra-low threshold. In addition we have analyzed the modified coupling properties in the UHQ regime where even weak scattering centers are sufficient to cause significant splitting of cavity modes into doublets. Modal coupling results in both finite reflection and a shift of the critical coupling point. Knowledge of this behavior is essential for proper calibration of Q and power build-up in UHQ devices.

Finally, as part of this review, a novel micro-cavity in the form of a microtoroid on-a-chip, which combines ultra-high-Q and wafer-scale processing, has been described. By merging the technology of wafer-scale fabrication with UHQ for the first time these devices address many of the drawbacks of previous STIMs and provide opportunities for integration of UHQ devices with other functions. In addition, they have inherent advantages over spherical cavities (such as a reduced cavity mode density and a reduced mode volume), which may facilitate the use and consideration of UHQ micro-resonators in many areas [89].One important outcome described in this chapter has been the realization of the first, microcavity parametric oscillator. Other exciting avenues in which a UHQ chip-based micro-cavity is particularly suitable is the study of light-matter interaction with Bose-Einstein condensates on a microelectronic chip [90] or for quantum information studies based on strong-coupling. This new integration capability could result in an entirely new class of 'lab on-a-chip' experiments designed to study fundamental processes. In addition the possibility of increasing functionality through use of microelectronic techniques such as ion-beam implantation can enable additional novel devices[91] and functions.

Acknowledgement

References

1.   Braginskii, V.B. and V.S. Ilchenko, *The Properties of the Optical Dielectric Microresonators.* Doklady Akademii Nauk Sssr, 1987. **293**(6): p. 1358-1361.

2.   Vernooy, D.W., V.S. Ilchenko, H. Mabuchi, E.W. Streed, and H.J. Kimble, *High-Q measurements of fused-silica microspheres in the near infrared.* Optics Letters, 1998. **23**(4): p. 247-249.

3.   Vernooy, D.W., A. Furusawa, N.P. Georgiades, V.S. Ilchenko, and H.J. Kimble, *Cavity QED with high-Q whispering gallery modes.* Physical Review A, 1998. **57**(4): p. R2293-R2296.

4.   Chang, R.K. and A.J. Campillo, *Optical processes in microcavities.* Advanced series in applied physics. Vol. 3. 1996, Singapore: World Scientific.

5.   Vahala, K.J., *Optical microcavities.* Nature, 2003. **424**(6950): p. 839-846.

6.   Sandoghdar, V., F. Treussart, J. Hare, V. LefevreSeguin, J.M. Raimond, and S. Haroche, *Very low threshold whispering-gallery-mode microsphere laser.* Physical Review A, 1996. **54**(3): p. R1777-R1780.

7.   Cai, M. and K. Vahala, *Highly efficient hybrid fiber taper coupled microsphere laser.* Optics Letters, 2001. **26**(12): p. 884-886.

8.   Spillane, S.M., T.J. Kippenberg, and K.J. Vahala, *Ultralow-threshold Raman laser using a spherical dielectric microcavity.* Nature, 2002. **415**(6872): p. 621-623.

9.   Qian, S.X., J.B. Snow, H.M. Tzeng, and R.K. Chang, *Lasing Droplets - Highlighting the Liquid-Air Interface by Laser-Emission.* Science, 1986. **231**(4737): p. 486-488.

10.   Qian, S.X. and R.K. Chang, *Multiorder Stokes Emission from Micrometer-Size Droplets.* Physical Review Letters, 1986. **56**(9): p. 926-929.

11.   Zhang, J.Z. and R.K. Chang, *Generation and Suppression of Stimulated Brillouin-Scattering in Single Liquid Droplets.* Journal of the Optical Society of America B-Optical Physics, 1989. **6**(2): p. 151-153.

12.   Lin, H.B. and A.J. Campillo, *Cw Nonlinear Optics in Droplet Microcavities Displaying Enhanced Gain.* Physical Review Letters, 1994. **73**(18): p. 2440-2443.

13.   Campillo, A.J., J.D. Eversole, and H.B. Lin, *Cavity Quantum Electrodynamic Enhancement of Stimulated- Emission in Microdroplets.* Physical Review Letters, 1991. **67**(4): p. 437-440.

14.   Vollmer, F., D. Braun, A. Libchaber, M. Khoshsima, I. Teraoka, and S. Arnold, *Protein detection by optical shift of a resonant microcavity.* Applied Physics Letters, 2002. **80**(21): p. 4057-4059.

15.   Oraevsky, A.N., *Whispering-gallery waves.* Quantum Electronics, 2002. **32**(5): p. 377-400.

16.   Michler, P., A. Kiraz, L.D. Zhang, C. Becher, E. Hu, and A. Imamoglu, *Laser emission from quantum dots in microdisk structures.* Applied Physics Letters, 2000. **77**(2): p. 184-186.

17.   Rabiei, P., W.H. Steier, C. Zhang, and L.R. Dalton, *Polymer micro-ring filters and modulators.* Journal of Lightwave Technology, 2002. **20**(11): p. 1968-1975.

18.   Armani, D.K., T.J. Kippenberg, S.M. Spillane, and K.J. Vahala, *Ultra-high-Q toroid microcavity on a chip.* Nature, 2003. **421**(6926): p. 925-928.

19.   Cai, M., O. Painter, and K.J. Vahala, *Observation of critical coupling in a fiber taper to a silica- microsphere whispering-gallery mode system.* Physical Review Letters, 2000. **85**(1): p. 74-77.

20.   Knight, J.C., G. Cheung, F. Jacques, and T.A. Birks, *Phase-matched excitation of whispering-gallery-mode resonances by a fiber taper.* Optics Letters, 1997. **22**(15): p. 1129-1131.

21.   Kippenberg, T.J., S.M. Spillane, and K.J. Vahala, *Modal coupling in traveling-wave resonators.* Optics Letters, 2002. **27**(19): p. 1669-1671.

22.   Spillane, S.M., T.J. Kippenberg, O.J. Painter, and K.J. Vahala, *Ideality in a fiber-taper-coupled microresonator system for application to cavity quantum electrodynamics.* Physical Review Letters, 2003. **91**(4): p. art. no.-043902.

23.   Kimble, H.J., *Strong interactions of single atoms and photons in cavity QED.* Physica Scripta, 1998. **T76**: p. 127-137.

24.   Min, B.K., T.J. Kippenberg, and K.J. Vahala, *Compact, fiber-compatible, cascaded Raman laser.* Optics Letters, 2003. **28**(17): p. 1507-1509.

25.   Stolen, R.H. and E.P. Ippen, *Raman Gain in Glass Optical Waveguides.* Applied Physics Letters, 1973. **22**(6): p. 276-278.

26.   Little, B.E., J.P. Laine, and H.A. Haus, *Analytic theory of coupling from tapered fibers and half-blocks into microsphere resonators.* Journal of Lightwave Technology, 1999. **17**(4): p. 704-715.

27.   Rayleigh, L. Scientific Papers, Cambrigde: Cambridge University. 617-620.

28.   Kippenberg, T.J., S.M. Spillane, D.K. Armani, and K.J. Vahala, *Fabrication and coupling to planar high-Q silica disk microcavities.* Applied Physics Letters, 2003. **83**(4): p. 797-799.

29.   Delfino, M. and T.A. Reifsteck, *Laser Activated Flow of Phosphosilicate Glass in Integrated- Circuit Devices.* Electron Device Letters, 1982. **3**(5): p. 116-118.

30.   McLachlan, A.D. and F.P. Meyer, *Temperature-Dependence of the Extinction Coefficient of Fused- Silica for Co2-Laser Wavelengths.* Applied Optics, 1987. **26**(9): p. 1728-1731.

31.   Serpenguzel, A., S. Arnold, and G. Griffel, *Excitation of Resonances of Microspheres on an Optical-Fiber.* Optics Letters, 1995. **20**(7): p. 654-656.

32.   Gorodetsky, M.L. and V.S. Ilchenko, *Optical microsphere resonators: optimal coupling to high-Q whispering-gallery modes.* Journal of the Optical Society of America B-Optical Physics, 1999. **16**(1): p. 147-154.

33.   Bouwmeester, D., A. Ekert, and A. Zeilinger, *The Physics of Quantum Information*, ed. Springer. 2000, Heidelberg.

34.   van Enk, S.J., J.I. Cirac, and P. Zoller, *Photonic channels for quantum communication.* Science, 1998. **279**(5348): p. 205-208.

35.   Duan, L.M., M.D. Lukin, J.I. Cirac, and P. Zoller, *Long-distance quantum communication with atomic ensembles and linear optics.* Nature, 2001. **414**(6862): p. 413-418.

36. Fiorentino, M., P.L. Voss, J.E. Sharping, and P. Kumar, *All-fiber photon-pair source for quantum communications.* Ieee Photonics Technology Letters, 2002. **14**(7): p. 983-985.

37. Mabuchi, H. and A.C. Doherty, *Cavity quantum electrodynamics: Coherence in context.* Science, 2002. **298**(5597): p. 1372-1377.

38. Pereira, S.F., Z.Y. Ou, and H.J. Kimble, *Quantum communication with correlated nonclassical states.* Physical Review A, 2000. **6204**(4): p. art. no.-042311.

39. Snyder, A.W. and J.D. Love, *Optical Waveguide Theory.* 2000: Kluwer Academic Publisher.

40. Haus, H.A., *Waves and fields in optoelectronics.* 1984, Englewood Cliffs: Prentice-Hall.

41. Weiss, D.S., V. Sandoghdar, J. Hare, V. Lefevreseguin, J.M. Raimond, and S. Haroche, *Splitting of High-Q Mie Modes Induced by Light Backscattering in Silica Microspheres.* Optics Letters, 1995. **20**(18): p. 1835-1837.

42. Gorodetsky, M.L., A.D. Pryamikov, and V.S. Ilchenko, *Rayleigh scattering in high-Q microspheres.* Journal of the Optical Society of America B-Optical Physics, 2000. **17**(6): p. 1051-1057.

43. Haus, H.A., *Electromagnetic fields and energy.* 1989, Englewood Cliff: Prentice Hall.

44. Gorodetsky, M.L., A.A. Savchenkov, and V.S. Ilchenko, *Ultimate Q of optical microsphere resonators.* Optics Letters, 1996. **21**(7): p. 453-455.

45. Braginskii, V.B., V.S. Ilchenko, and M.L. Gorodetskii, *Optical Microresonators with the Modes of the Whispering Gallery Type.* Uspekhi Fizicheskikh Nauk, 1990. **160**(1): p. 157-159.

46. Buck, J.R. and H.J. Kimble, *Optimal sizes of dielectric microspheres for cavity QED with strong coupling.* Physical Review A, 2003. **67**(3): p. art. no.-033806.

47. Schiller, S., *Asymptotic-Expansion of Morphological Resonance Frequencies in Mie Scattering.* Applied Optics, 1993. **32**(12): p. 2181-2185.

48. Collot, L., V. Lefevreseguin, M. Brune, J.M. Raimond, and S. Haroche, *Very High-Q Whispering-Gallery Mode Resonances Observed on Fused-Silica Microspheres.* Europhysics Letters, 1993. **23**(5): p. 327-334.

49.   Raman C.V., K.K.S., *A new type of secondary radiation.* Nature, 1928(121): p. 501.

50.   Bloembergen, N. and Y.R. Shen, *Coupling between Vibrations + Light Waves in Raman Laser Media.* Physical Review Letters, 1964. **12**(18): p. 504-&.

51.   Gaubatz, U., P. Rudecki, M. Becker, S. Schiemann, M. Kulz, and K. Bergmann, *Population Switching between Vibrational Levels in Molecular- Beams.* Chemical Physics Letters, 1988. **149**(5-6): p. 463-468.

52.   Bergmann, K., H. Theuer, and B.W. Shore, *Coherent population transfer among quantum states of atoms and molecules.* Reviews of Modern Physics, 1998. **70**(3): p. 1003-1025.

53.   Boyd, R.W., *Nonlinear optics*. 1992, Boston: Academic Press.

54.   Ippen, E.P. and R.H. Stolen, *Stimulated Brillouin-Scattering in Optical Fibers.* Applied Physics Letters, 1972. **21**(11): p. 539-&.

55.   Stolen, R.H., *Fiber Raman Lasers.* Fiber and Integrated Optics, 1980. **3**(1): p. 21-52.

56.   Brasseur, J.K., K.S. Repasky, and J.L. Carlsten, *Continuous-wave Raman laser in H-2.* Optics Letters, 1998. **23**(5): p. 367-369.

57.   Agrawal, G.P., *Nonlinear fiber optics*. 1989, Boston: Academic Press.

58.   Stolen, R.H., A.R. Tynes, and E.P. Ippen, *Raman Oscillation in Glass Optical Waveguide.* Applied Physics Letters, 1972. **20**(2): p. 62-&.

59.   Lin, H.B. and A.J. Campillo, *Microcavity enhanced Raman gain.* Optics Communications, 1997. **133**(1-6): p. 287-292.

60.   Matsko, A.B., A.A. Savchenkov, R.J. Letargat, V.S. Ilchenko, and L. Maleki, *On cavity modification of stimulated Raman scattering.* Journal of Optics B-Quantum and Semiclassical Optics, 2003. **5**(3): p. 272-278.

61.   Stolen, R.H. and J.E. Bjorkholm, *Parametric Amplification and Frequency-Conversion in Optical Fibers.* Ieee Journal of Quantum Electronics, 1982. **18**(7): p. 1062-1072.

62.   Gaeta, A.L., *Catastrophic collapse of ultrashort pulses.* Physical Review Letters, 2000. **84**(16): p. 3582-3585.

63.   Dabby, F.W. and J.R. Whinnery, *Thermal Self-Focusing of Laser Beams in Lead Glasses.* Applied Physics Letters, 1968. **13**(8): p. 284-&.

64.   Walls, D.F. and G.J. Milburn, *Quantum Optics*. 1994, New York: Springer.

65.   Scully, M.O. and M.S. Zubairy, *Quantum Optics*. 1996: Cambridge.

66.   Uetake, S., M. Katsuragawa, M. Suzuki, and K. Hakuta, *Stimulated Raman scattering in a liquid-hydrogen droplet.* Physical Review A, 2000. **6001**(1): p. art. no.-011803.

67.   Stevenson, R.M., V.N. Astratov, M.S. Skolnick, D.M. Whittaker, M. Emam-Ismail, A.I. Tartakovskii, P.G. Savvidis, J.J. Baumberg, and J.S. Roberts, *Continuous wave observation of massive polariton redistribution by stimulated scattering in semiconductor microcavities.* Physical Review Letters, 2000. **85**(17): p. 3680-3683.

68.   Tartakovskii, A.L., M.S. Skolnick, D.N. Krizhanovskii, V.D. Kulakovskii, R.M. Stevenson, R. Butte, J.J. Baumberg, D.M. Whittaker, and J.S. Roberts, *Stimulated polariton scattering in semiconductor microcavities: New physics and potential applications.* Advanced Materials, 2001. **13**(22): p. 1725-1730.

69.   Butte, R., M.S. Skolnick, D.M. Whittaker, D. Bajoni, and J.S. Roberts, *Dependence of stimulated scattering in semiconductor microcavities on pump power, angle, and energy.* Physical Review B, 2003. **68**(11): p. art. no.-115325.

70.   Braginsky, V.B., M.L. Gorodetsky, and V.S. Ilchenko, *Quality-Factor and Nonlinear Properties of Optical Whispering- Gallery Modes.* Physics Letters A, 1989. **137**(7-8): p. 393-397.

71.   Treussart, F., V.S. Ilchenko, J.F. Roch, J. Hare, V. Lefevre-Seguin, J.M. Raimond, and S. Haroche, *Evidence for intrinsic Kerr bistability of high-Q microsphere resonators in superfluid helium.* European Physical Journal D, 1998. **1**(3): p. 235-238.

72.   Golovchenko, E., P.V. Mamyshev, A.N. Pilipetskii, and E.M. Dianov, *Mutual Influence of the Parametric Effects and Stimulated Raman-Scattering in Optical Fibers.* Ieee Journal of Quantum Electronics, 1990. **26**(10): p. 1815-1820.

73.   Sharping, J.E., M. Fiorentino, P. Kumar, and R.S. Windeler, *Optical parametric oscillator based on four-wave mixing in microstructure fiber.* Optics Letters, 2002. **27**(19): p. 1675-1677.

74.   Russell, P., *Photonic crystal fibers.* Science, 2003. **299**(5605): p. 358-362.

75.   Slusher, R.E., L.W. Hollberg, B. Yurke, J.C. Mertz, and J.F. Valley, *Observation of Squeezed States Generated by 4-Wave Mixing in an Optical Cavity.* Physical Review Letters, 1985. **55**(22): p. 2409-2412.

76.   Shelby, R.M., M.D. Levenson, S.H. Perlmutter, R.G. Devoe, and D.F. Walls, *Broad-Band Parametric Deamplification of Quantum Noise in an Optical Fiber.* Physical Review Letters, 1986. **57**(6): p. 691-694.

77.   Levenson, M.D., R.M. Shelby, A. Aspect, M. Reid, and D.F. Walls, *Generation and Detection of Squeezed States of Light by Nondegenerate 4-Wave Mixing in an Optical Fiber.* Physical Review A, 1985. **32**(3): p. 1550-1562.

78.   Silberhorn, C., P.K. Lam, O. Weiss, F. Konig, N. Korolkova, and G. Leuchs, *Generation of continuous variable Einstein-Podolsky-Rosen entanglement via the Kerr nonlinearity in an optical fiber.* Physical Review Letters, 2001. **86**(19): p. 4267-4270.

79.   Sizmann, A. and G. Leuchs, *The optical Kerr effect and quantum optics in fibers*, in *Progress in Optics, Vol Xxxix*. 1999. p. 373-469.

80.   Wang, L.J., C.K. Hong, and S.R. Friberg, *Generation of correlated photons via four-wave mixing in optical fibres.* Journal of Optics B-Quantum and Semiclassical Optics, 2001. **3**(5): p. 346-352.

81.   Fujiwara, T., D. Wong, Y. Zhao, S. Fleming, S. Poole, and M. Sceats, *Electrooptic Modulation in Germanosilicate Fiber with Uv- Excited Poling.* Electronics Letters, 1995. **31**(7): p. 573-575.

82.   Myers, R.A., N. Mukherjee, and S.R.J. Brueck, *Large 2nd-Order Nonlinearity in Poled Fused-Silica.* Optics Letters, 1991. **16**(22): p. 1732-1734.

83.   Polzik, E.S., J. Carri, and H.J. Kimble, *Spectroscopy with Squeezed Light.* Physical Review Letters, 1992. **68**(20): p. 3020-3023.

84.   Heidmann, A., R.J. Horowicz, S. Reynaud, E. Giacobino, C. Fabre, and G. Camy, *Observation of Quantum Noise-Reduction on Twin Laser-Beams.* Physical Review Letters, 1987. **59**(22): p. 2555-2557.

85.   Zhang, K.S., T. Coudreau, M. Martinelli, A. Maitre, and C. Fabre, *Generation of bright squeezed light at 1.06 mu m using cascaded nonlinearities in a triply resonant cw periodically-poled lithium niobate optical parametric oscillator.* Physical Review A, 2001. **6403**(3): p. art. no.-033815.

86.   Saleh, B.E.A., B.M. Jost, H.B. Fei, and M.C. Teich, *Entangled-photon virtual-state spectroscopy.* Physical Review Letters, 1998. **80**(16): p. 3483-3486.

87.   Yang, L. and K.J. Vahala, *Gain functionalization of silica microresonators.* Optics Letters, 2003. **28**(8): p. 592-594.

88.   L. Yang, D.K.A., and K. J. Vahala, *Fiber-coupled erbium microlasers on a chip.* Appl. Phys. Lett., 2003. **83**: p. 825.

89.   Gerard, J.M., *Quantum optics - Boosting photon storage.* Nature Materials, 2003. **2**(3): p. 140-141.

90.   Hansel, W., P. Hommelhoff, T.W. Hansch, and J. Reichel, *Bose-Einstein condensation on a microelectronic chip.* Nature, 2001. **413**(6855): p. 498-501.

91.   Polman, A., B. Min, J. Kalkman, T.J. Kippenberg, and K.J. Vahala, *Ultralow-threshold erbium implanted toroidal microlaser on silicon.* Applied Physics Letters, 2004. **84**(7): p. 1037.